ADVANCED MATERIALS
www.advmat.de

Electro-Thermal Characterization of Dynamical VO_2 Memristors via Local Activity Modeling

Timothy D. Brown, Stephanie M. Bohaichuk, Mahnaz Islam, Suhas Kumar, Eric Pop, and R. Stanley Williams*

Translating the surging interest in neuromorphic electronic components, such as those based on nonlinearities near Mott transitions, into large-scale commercial deployment faces steep challenges in the current lack of means to identify and design key material parameters. These issues are exemplified by the difficulties in connecting measurable material properties to device behavior via circuit element models. Here, the principle of local activity is used to build a model of VO_2/SiN Mott threshold switches by sequentially accounting for constraints from a minimal set of quasistatic and dynamic electrical and high-spatial-resolution thermal data obtained via in situ thermoreflectance mapping. By combining independent data sets for devices with varying dimensions, the model is distilled to measurable material properties, and device scaling laws are established. The model can accurately predict electrical and thermal conductivities and capacitances and locally active dynamics (especially persistent spiking self-oscillations). The systematic procedure by which this model is developed has been a missing link in predictively connecting neuromorphic device behavior with their underlying material properties, and should enable rapid screening of material candidates before employing expensive manufacturing processes and testing procedures.

1. Introduction

One promising strategy to counter the end of Moore's law scaling is through the exploitation of nonlinear dynamics in neuromorphic devices,[1] particularly those induced by the insulator–metal transition (IMT) in VO_2 and other thermal oxides.[2] Despite substantial progress in demonstrating neuronal behaviors: action potential spiking, plasticity, potentiation and depression,[3] the state-of-the-art has not yet advanced to the point of designing neuromorphic circuitry beyond small numbers of nonlinear components. This issue is partly due to the substantial difficulty and cost involved in characterizing and modeling a single neuromorphic element, much less an interacting network of such elements.[4] Furthermore, the crucial links between material properties and desired neuromorphic behavior are only just being forged.[5] For example, it is understood that nonlinear switching is required to induce sustained dynamical signals, but how large of an electrical switching ratio is required, how hysteresis in the switching affects these signals, and how materials properties like electrical and thermal conductivity affect DC power requirements, are all open questions. Without answers to these questions, crucial design decisions like what material should be used, what processing can optimize its electrical transport in what way, and what level of device or circuit performance can be expected, become equally matters of art as well as science.[6]

The first difficulty of modeling networks of nonlinear dynamical devices has been addressed using compact modeling, which aims to capture the behavior of individual devices across the full range of relevant physical conditions within a small set of lumped model parameters.[7] Such modeling is accomplished through a careful compromise of just-sufficient fidelity with physics-based intuition; compact models are neither expensive high-fidelity molecular dynamics simulations nor naïve empirical fits of current–voltage curves that change for each new data set. Instead, compact models for memristors comprise physically reasonable transport models paired with relevant dynamical equations,[7b] and the wealth of nonlinear behavior, e.g., negative differential resistance (NDR), oscillations, and instability arises naturally from the interaction of these two ingredients. Chua's theory of local activity underlies the entire capability and limitations for compact modeling of nonlinear dynamical systems.[8] Recent recontextualization of the local activity theory has streamlined its use as a design tool.[5a,9] It is now understood that instabilities leading to NDR, but not all instabilities, can produce sustained dynamical behaviors like self-oscillation. Furthermore, experimentally observed

T. D. Brown, R. S. Williams
Department of Electrical and Computer Engineering
Texas A&M University
College Station, TX 77843, USA
T. D. Brown, S. Kumar
Sandia National Laboratories
Livermore, CA 94550, USA
E-mail: su1@alumni.stanford.edu
S. M. Bohaichuk, M. Islam, E. Pop
Department of Electrical Engineering
Stanford University
Stanford, CA 94305, USA
E. Pop
Department of Materials Science and Engineering
Stanford University
Stanford, CA 94305, USA
The ORCID identification number(s) for the author(s) of this article can be found under https://doi.org/10.1002/adma.202205451.

DOI: 10.1002/adma.202205451

dynamics may result from coupling a nonlinear device to an external, potentially off-chip, component. Compact modeling must take account of the external characterization instruments, as well as the device under test itself.[10]

Predictive compact models have now been constructed for several thermal oxide materials,[11] yet the crucial comparisons for material selection have not yet been performed. What is needed is a synthesis of the compact modeling framework with material-dependent model parameters in a unified framework. In general, this is a costly proposition. Typically, only a handful of champion devices are capable of desired neuromorphic behaviors and worth the effort of modeling. Furthermore, the experimental effort required to characterize a device is costly, since both electrical transport and the dynamical equations are dependent on one or more state variables, and one generally attempts to capture this complete dependence. There is not yet a systematic roadmap for what data needs to be collected when to construct the model, and model fitting often turns out to be a lengthy exercise in guess-and-check tuning, as opposed to automated parametric fitting.

The difficulty of constructing material-based compact models can be eased by two realizations. First, the interaction between nonlinear device and external circuitry can be subtle, e.g., the absence of dynamical behavior may equally be caused by misalignment of the external circuit impedances as by a damaged device. Experimentalists may have many more good devices at their disposal than initially realized, if external degrees of freedom can be intelligently utilized. Second, a deeper understanding of the local activity theory can help constrain the data needed to construct a compact model. Ultimately, all that is required is a state variable, a state-dependent conductance, and enough dynamical data to model the dynamical state equations. In this sense, steady-state NDR and oscillations are not only evidence of desired dynamical behaviors, but also important constraints to defining a data set for modeling.

Here, we approach the challenge of constructing a compact model for lateral VO_2 memristors (**Figure 1**a) directly, at each subsequent stage exploiting the collected experimental data to the maximum extent to constrain the model parameters. Using in situ thermoreflectance mapping under steady-state electrical bias (Figure 1b), we obtain a complete set of steady-state temperature–current–voltage measurements, simultaneously observing NDR, instability, and oscillations. We synthesize data sets for multiple devices with varying dimensions from across a chip, demonstrating sufficient qualitative similarity to explain quantitative dissimilarity within the context of simple scaling laws. At every step, we place the data within the context of local activity theory, using derived equations to fit the data and parameterize the compact model using systematic least-squares procedures that provide accurate values and uncertainties of model parameters, including inferring an external circuit capacitance (**Figure 2**b, C_{eff}) from dynamical data. The result is a material-dependent compact model for VO_2, fit systematically using automatic optimization routines, and verified against large sets of quasi-static and dynamical data for devices of varying dimensions. In so doing, we develop the first effort toward understanding the links between electro-thermal nonlinearities and desired neuromorphic behaviors, and simultaneously verify the principles of local activity as recontextualized in recent theoretical work.

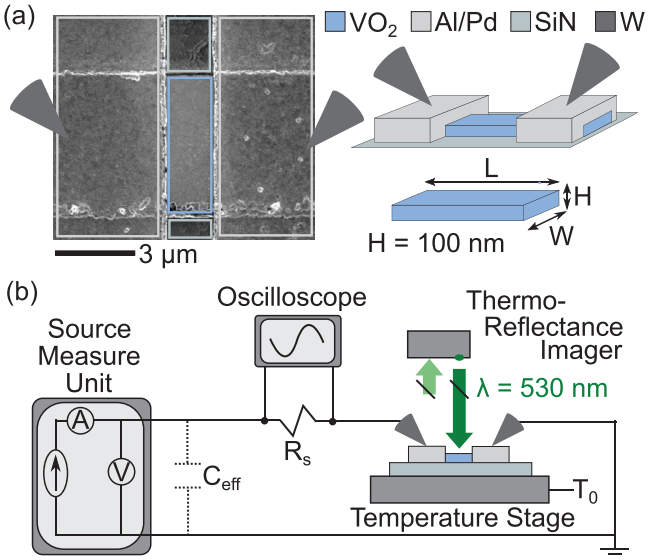

Figure 1. VO_2 device structure and in situ thermoreflectance characterization. a) Top-down SEM image of a lateral device comprising an etched VO_2 channel on a SiN substrate underneath Al/Pd contacts and W probes, together with an isometric schematic and definition of the dimensions (L,W,H) as used in this work. b) Elements of in situ thermoreflectance technique to simultaneously measure steady-state current–voltage–temperature and oscillations. Oscillations are measured across a limiter resistor R_s to prevent changes in oscilloscope loading as the device impedance changes, and they are induced by the interaction of an effective electrical capacitance C_{eff} with the memristor nonlinearities.

Several challenges and surprises arise along the way. First, the presence of a localized hot channel in each memristor complicates the idealized compact model picture, which contains no spatial coordinates and thus no variation in the physical variables throughout the device volume.[12] This exposes an essential limitation of compact models and necessitates partitioning the device into intra-channel and extra-channel volumes such that within each, a lumped compact device model applies. Second, during electro-thermal characterization to develop the compact model, we discovered an unexpected peak in the interfacial thermal conductivity near the martensitic M1 → R transformation. This quickly varying thermal conductivity is the main source of apparent electrical hysteresis in the steady-state current–voltage curve, which has been shown to mimic neural dynamics.[11b] This discovery uncovers an as-yet unexplained physical mechanism that negates the contribution to the thermal conductivity due to the increase in carrier concentration across the IMT.

Overall, our modeling methods demonstrate a systematic procedure to derive meaningful material parameters from experimentally inexpensive quasi-DC I–V characterization and oscillation data, and our results reveal the essential material properties of VO_2/SiN devices underlying neuromorphic behavior, namely, a rapidly increasing electrical conductivity coupled with a peaked, rapidly changing thermal conductivity. This work lays the foundation for future studies in engineered VO_2 and/or other promising materials systems linking their electro-thermal properties to local activity and desired materials properties, to eventually enable definite materials selection principles for these applications.

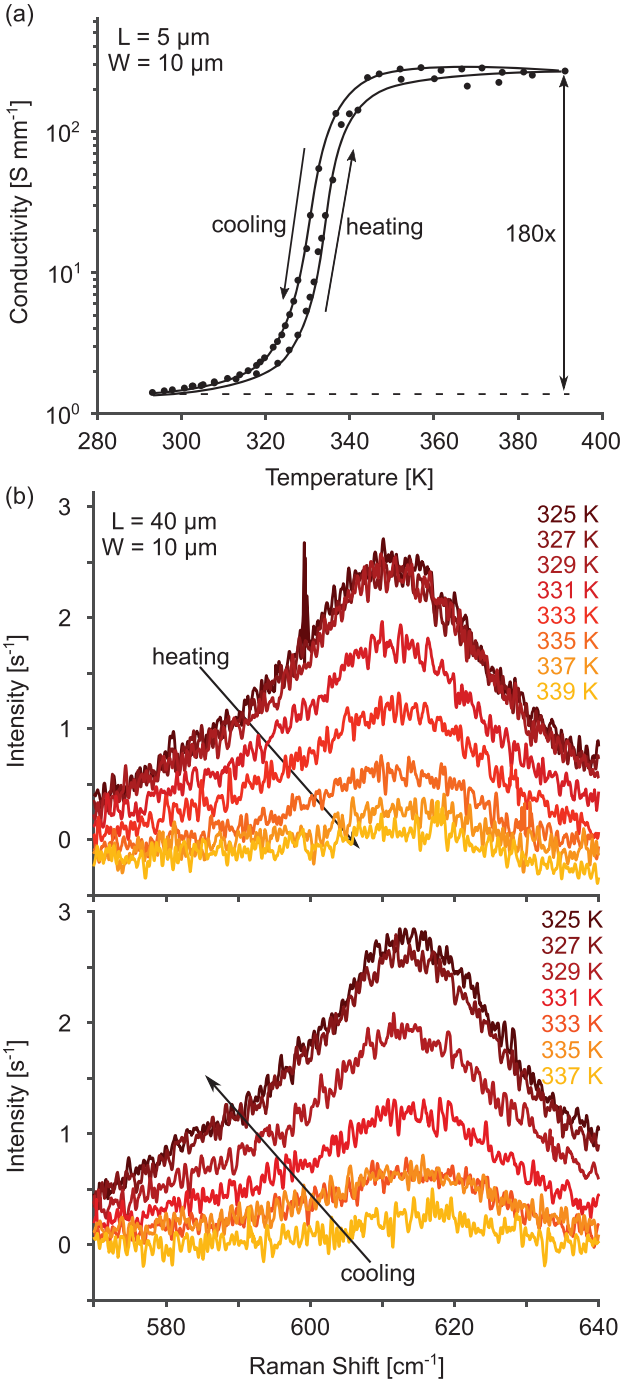

Figure 2. Characterization of the first-order phase transformation in lateral VO_2. a) Electrical conductivity as a function of temperature increased by two orders of magnitude on heating through $T \approx 330$–340 K in device with ($L = 5$ µm, $W = 10$ µm). Uncertainties (standard deviation of three linear I–V measurements, $0 \leq V \leq 50$ mV) are less than 1.5 S mm^{-1}. b) The Raman-active monoclinic M1 phase peak decreased on transformation to rutile R phase when heating through the same temperature range. Raman data were taken on a 40 µm-length device to ensure no overlap between the laser spot and Al/Pd top contacts. Additional conductivity characterization as in (a) is in Figure S2 (Supporting Information).

2. Results

2.1. Material Characterization

VO_2 film quality was first confirmed electrically through isothermal electrical conductivity characterization of the insulator–metal transition (IMT) in lateral device structures. The IMT showed repeatable conductivity switching of ≈200× across a critical temperature of 335 K (Figure 2a). Large positive conductivity switching and the observed thermal hysteresis of ≈10 K are in good agreement with literature values for undoped VO_2.[13] Devices of varying dimensions across a chip were characterized (Figure S2, Supporting Information), with variations in switching ratios less than 10% between devices located nearby on the chip, although the variation across the entire chip area was substantial (from 100 × to 220 ×). This suggests some nominal variation in material and device properties across the 1 cm^2 chip area, likely variations in elemental composition or in effective device volume due to lithographic edge effects.

The presence of a crystallographic first-order phase transformation (FOPT) accompanying the IMT was independently confirmed with temperature-dependent Raman spectroscopy (Figure 2b) on a second device with the same width. The longer device dimension was useful to prevent the laser spot from overlapping contact pads. The M1 monoclinic Raman peak at 618 cm^{-1} was observed to decrease systematically on heating, then increase to the same level on cooling, indicating a reversible structural phase transformation from the monoclinic M1 to the rutile R phase. The transformation temperatures estimated from the Raman data, i.e., M1 → R initiation and completion temperatures of (329 K, 339 K), and R → M1 temperatures of (337 K, 327 K) agreed closely with values from conductivity–temperature curves.

2.2. Quasi-DC Current–Voltage Characterization

Dynamical behavior in nonlinear devices, like self-oscillation and spiking, is intimately connected to negative differential resistance (NDR) in quasi-steady-state current–voltage curves.[5a,9,14] Continuous current-sourced current–voltage (I–V) sweeps were obtained for lateral VO_2 memristors with various dimensions across the chip (**Figure 3**) using a commercial high-resolution source measure unit (SMU). An important factor was that the current-sourced I–V curves must be measured with a limiter resistor in series before the device under test (Figure 1b; Figure S3, Supporting Information), and different limiters are required for different device dimensions. All data collection, including continuous and pointwise I–V sweeps, in situ thermoreflectance, and recording of self-oscillations was done using the same limiter resistor for a given device. The reason behind this is a complete story in itself, with interactions between electrical instabilities, self-oscillations, resistive damping, and the average device conductance at a given bias point all playing a major role. For this work, we will simply observe that for every device dimension there was a small range of limiter resistors large enough to damp the amplitude of extreme thermal self-oscillations while not suppressing them entirely. The I–V curves have been measured under this optimized condition for all the

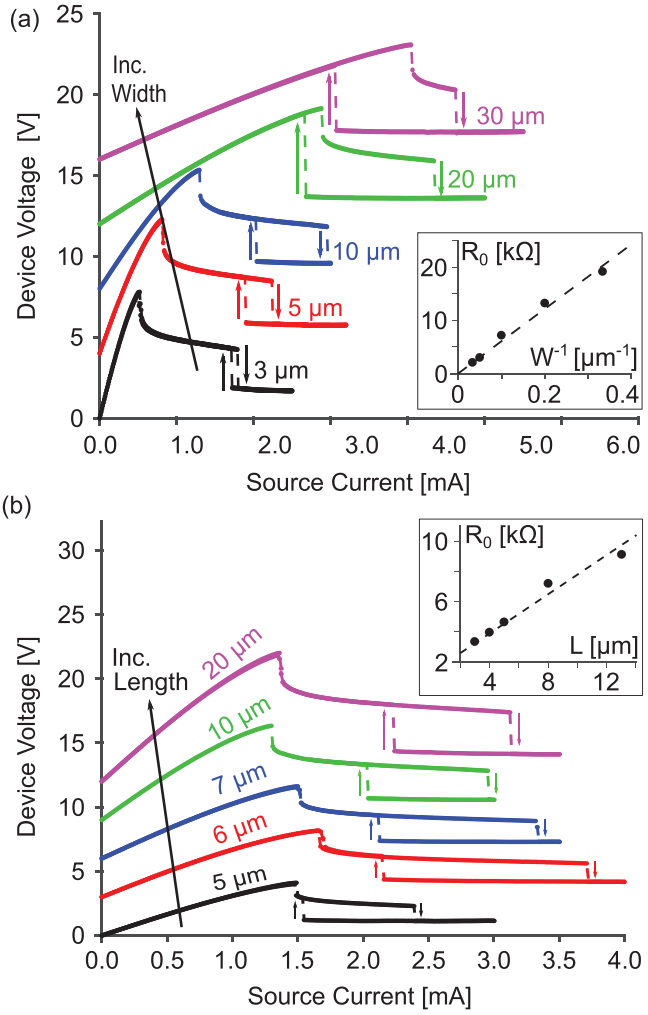

Figure 3. a,b) Measured quasi-DC *I–V* characterization for lateral VO_2 memristors of varying width at fixed 10 μm length (a) and length at fixed 10 μm width (b). Limiting series resistors R_s (Figure S3, Supporting Information) were adjusted to be small enough to enable characterization of PDR, NDR, and box-like hysteresis in the same *I–V* sweep, but large enough to damp large amplitude electro-thermal oscillations and prevent device self-damage. Memristor voltage was calculated from the measured supply voltage by subtracting the voltage drop IR_s across the series resistor. The curves were vertically offset for clarity; without the offset all curves pass through the origin. Uncertainties (manufacturer specifications) are 3 mV, 0.1 μA. (Insets) Tangent device resistances dV/dI near the origin agree well with dimensional scaling $R_0 \sim L/W$. Uncertainties (Jacobian of fit) are less than 5 Ω.

devices in this work. Under these conditions, all memristors manifested qualitatively similar *I–V* behavior, with a positive differential resistance (PDR, as distinct from NDR) region passing through the origin followed by a sharp cusp leading into a substantial NDR region (Figure 3).

The NDR was followed by a hysteretic box-shaped region, such that the drop in the voltage on the forward current sweep (Figure 3, down arrows) was offset to higher currents with respect to the corresponding voltage increase on the reverse sweep (Figure 3, up arrows). Obvious major differences among the *I–V* curves for various devices were the slopes of the initial PDR regions (Figure 3, insets), which were consistent with typical dimensional resistance scaling,

$$\left(\frac{dV}{dI}\right)_{I\to 0} \equiv R_0 = \rho\frac{L}{WH} \quad (1)$$

where ρ is electrical resistivity, L is the length dimension parallel to electrical flow, and W and H are the width and height/thickness dimensions defining the area normal to electrical flow (Figure 1a).

The adherence of the PDR data to the scaling law Equation (1) suggests both that the electrical resistivity (equivalently, conductivity) was approximately constant for all devices in the PDR region, and also that the current density through the devices was spatially uniform, so that the effective conduction dimensions are identical to the device dimensions. A second major difference between the *I–V* curves was the relationship between the reverse hysteresis threshold (Figure 3, up arrows) and the PDR or NDR regions. In narrow devices (small W), the reverse hysteresis threshold was well within the NDR region; whereas in wider devices, the reverse threshold was below the NDR onset in the PDR region. Finally, there were differences in the relationship between the NDR onset and forward hysteresis threshold (Figure 3, down arrows), leading to dimension-dependent NDR current intervals. In all cases, despite quantitative differences, there was qualitative agreement in the shapes and features of the quasistatic *I–V* curves among the various memristors, and the difference between PDR regions was consistent with dimensional resistance scaling. This provided an impetus to explain the behavior of all devices with a single set of material-dependent model parameters.

2.3. Simultaneous Measurements of Oscillations and Thermoreflectance

Quasistatic NDR is an inherent signature of instability and local activity, and under the proper conditions can lead to electrical (and thermal) self-oscillation.[5a] In situ self-oscillations during continuous *I–V* measurements using current sweeps were observed for all devices, independent of device dimension, within their NDR region. In all cases, the oscillations were observed to begin abruptly, at finite amplitude and frequency, right after the boundary between PDR and NDR, with the oscillation frequencies increasing about an order of magnitude through the NDR region, before abruptly ending at the sudden voltage drop marking the forward hysteresis threshold. On the reverse sweep, oscillations were suppressed in all memristors up to the reverse hysteresis threshold. Then, if the devices had a reverse threshold below the NDR onset, reaching the reverse hysteresis threshold caused the *I–V* state to jump back into the initial PDR region where oscillations could not occur. For memristors for which the NDR onset was below the reverse hysteresis threshold, reaching the reverse hysteresis threshold would cause the system to jump back into the NDR region, and oscillations were observed just as for the forward sweep in the NDR region.

The dynamical behavior of a particular memristor was probed further using a second benchtop SMU with better tolerance to repeated load switching at fixed bias (Experimental

Section) to make simultaneous pointwise quasistatic *I–V* measurements while recording the oscillation traces over ≈1 million cycles (**Figure 4**). Current oscillations were determined by dividing voltage oscillations across the series limiter resistor by its resistance, thereby ensuring the oscilloscope would not suffer loading effects from the rapidly changing device impedance (Figure 1). An important observation enabled by the pointwise measurement was that both the voltage and current decreased after the forward hysteresis threshold (Figure 4a, red arrow) from (3.56 ± 0.01 mA, 3.70 ± 0.01 V) at point A to (3.40 ± 0.01 mA, 2.39 V) at point B. In contrast to SMUs designed for continuous sweeping, which can have arbitrarily small, ever-increasing current steps, the benchtop SMU step size is limited by the resolution of the particular source/measure range and therefore, leads to some overshoot and settling. The interaction between the overshoot and inherent instability at the forward hysteresis threshold enabled observation of the simultaneous decrease in current and voltage after the forward hysteresis. Each datum in the pointwise curve is an average of >4 triggered measurements over one minute at fixed setpoint (see Experimental Section).

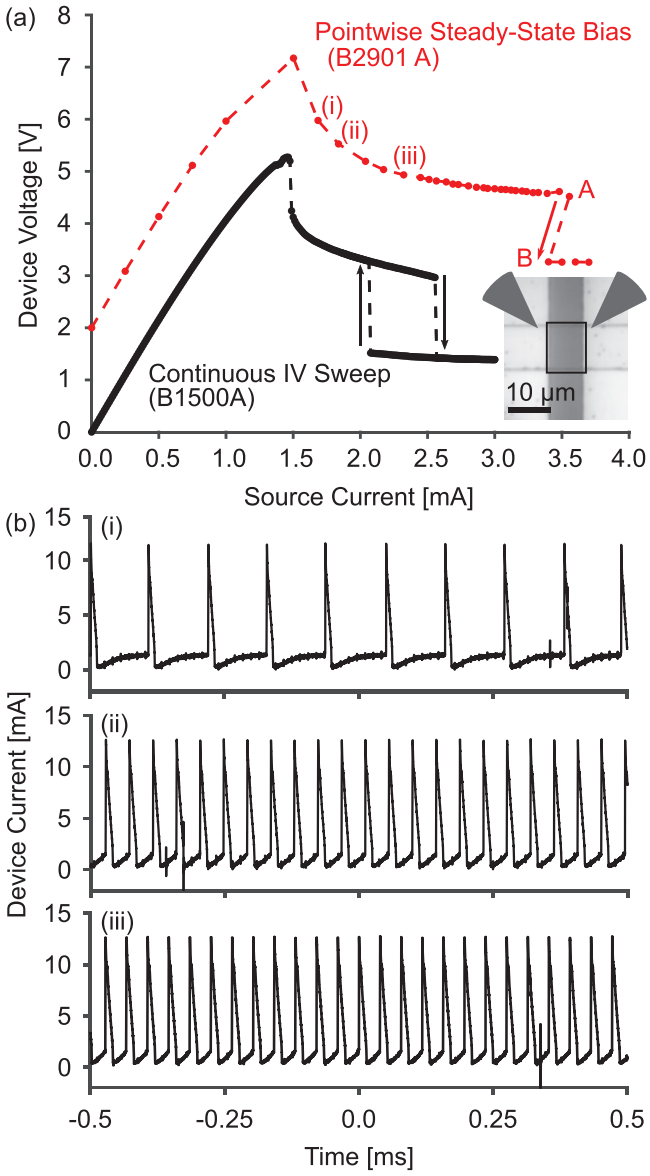

Figure 4. a) Room-temperature quasi-DC *I–V* sweeps (black, continuous sweep with B1500A mainframe SMU; red, pointwise sweep with B2901A benchtop SMU) on a lateral VO_2 memristor (L = 8 µm, W = 10 µm). The current and voltage simultaneously decrease at the forward hysteresis threshold in the pointwise sweep (red arrow from A to B). Pointwise *I–V* sweep (a,red) vertically offset for clarity. For black data, uncertainties (manufacturer specification) are 3 mV, 0.1 µA; for red data (standard deviation of four spot measurements) they are less than 15 µA, 20 mV. Pointwise sweep is more favorable for thermoreflectance characterization (Figure 5), which was obtained simultaneously with oscillation data. b) Selected current self-oscillations observed at three distinct current bias points (i), (ii), (iii) in the NDR region. Uncertainties (20 mV noise floor/330 Ω) are 0.06 mA.

Simultaneously, a calibrated steady-state thermoreflectance technique (Figure S4, Supporting Information) was used to obtain thermal maps of the entire memristor area under current bias, again for every point on the pointwise *I–V* curve in Figure 4a. A selection from this collection of thermal maps is displayed in **Figure 5**a. The limitations of the thermoreflectance technique prevented accurate temperature measurement for <334 K or >353 K.

The rectangular areas in Figure 5a correspond to the entire memristor area, i.e., the emphasized area in the optical image in Figure 4a inset. The thermal maps clearly show a significant temperature contrast between a ≈3 µm wide hot channel and the cooler exterior surrounding the channel. The hot conduction channel extends across the entire 10 µm length of the memristor. Such a localization of current density and Joule heating within an NDR region was first predicted by Ridley,[15] and has since been confirmed in VO_2 and NbO_2 and interpreted in terms of global minimization of thermodynamic potentials.[12,16] This localization establishes that a pure lumped model cannot fully capture the device physics and therefore must be modified. Instead, there is a natural decomposition of the memristor volume into intra-channel and extra-channel volumes, which here forms the basis for the bipartite model developed in Section 3.

Each thermal map was post-processed to systematically compute a characteristic intra-channel temperature and uncertainty. First, an autocorrelation was used to straighten out any slight curvature in the channels along the length dimension. Second, the straightened thermal map was averaged along the length dimension to obtain a statistical distribution of channel temperature along the width dimension (Figure 5b, inset). Although there is some typical variation in the peak channel temperature of 0.3 K along the horizontal direction, this variation was dominated by the height of the peak above the baseline and the qualitative peak shape is evident. Finally, a Gaussian distribution was fit to each temperature versus distance curve to determine a peak channel temperature (Figure 5b) and effective channel width (Figure 5c)

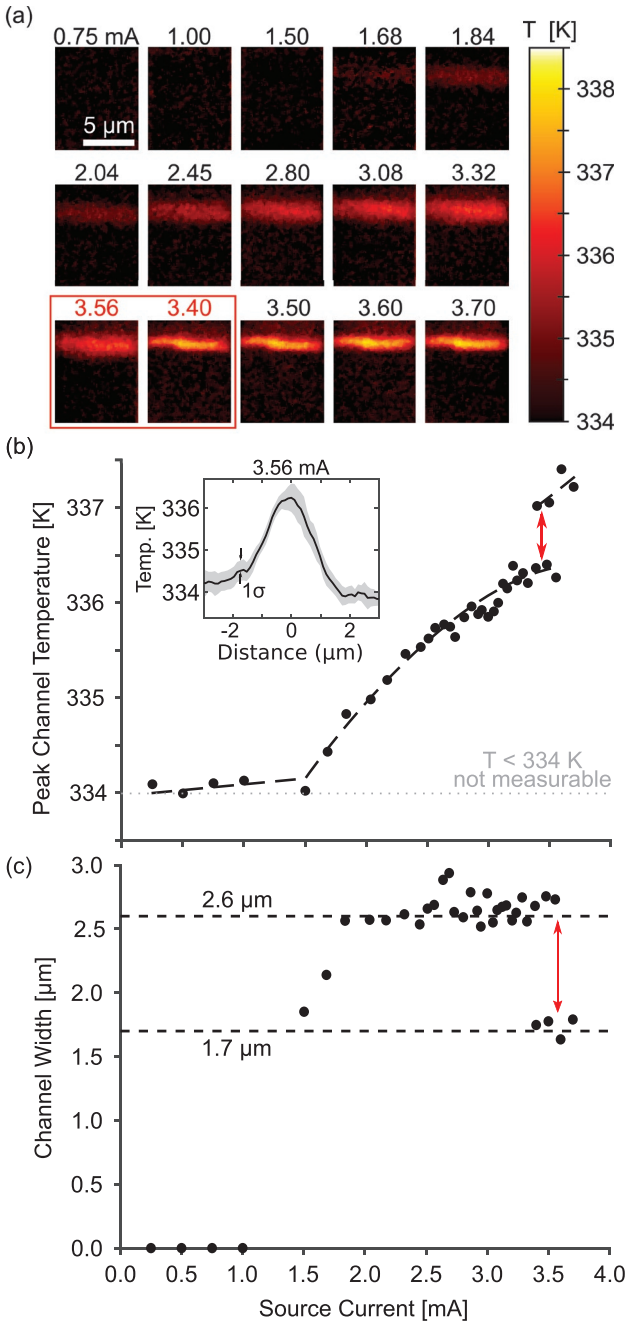

Figure 5. Thermal characterization of the VO_2 lateral memristor ($L = 8$ µm, $W = 10$ µm) in Figure 4. a) Selected steady-state thermoreflectance maps, b) peak channel temperatures, and c) effective channel widths at the current biases of the pointwise I–V sweeps (Figure 4a). The red box in (a) marks the boundary of the channel width and temperature discontinuity (red arrows) in (b) and (c) corresponding to the simultaneous current and voltage decrease in Figure 4a. Inset: Example of autocorrelated and averaged cross-section of temperature distribution along device width dimension at 3.56 mA bias. Uncertainties in source current are less than 15 µA, as in Figure 4a. Uncertainties in peak temperature and channel width (standard deviation of three consecutive spot measurements) are less than 0.06 K, 0.03 µm.

corresponding to each bias point. Gaussian fits were obtained for three consecutive thermal maps and the fit parameters were averaged to yield a final peak temperature with uncertainty.

Table 1. Observed channel widths as function of channel temperature summarized from data in Figure 5. In this work, these values are empirical model parameters determined solely by experiment, and are required for the model decomposition in Section 4.2.

Channel Width w_{chan} as Function of Steady State Bias		
Domain	Measured Value [µm]	Uncertainty [µm]
$T < 336.5$ K	2.6	±0.1
$T > 336.5$ K	1.7	±0.1

Hence, quasi-DC bias current and voltage, oscillation traces, and channel temperature and width were all obtained simultaneously during the pointwise I–V measurements in Figure 4a.

The clear monotonic increase in channel temperature with increasing bias is consistent with Joule self-heating, and confirms that internal temperature(s) is the primary state variable leading to instability, NDR, and oscillation. The Gaussian fits also revealed that the channel width was approximately constant throughout the NDR region (**Table 1**), but suddenly decreased at the forward electrical hysteresis threshold (Figure 5c), along with a corresponding discontinuous increase in temperature. Hence, the forward hysteresis threshold marked a point where the current and voltage simultaneously decreased and the channel temperature increased. The discontinuity in current, voltage, and temperature is a signature of inaccessible locally active PDR within the apparent hysteresis in the I–V plots, as will be discussed in Section 4.3.

3. Model Construction

3.1. Local Activity Theory: NDR, Nonlinearity, and Oscillations

Leon Chua has created a general framework for describing the behavior of nonlinear circuit elements in terms of the dynamical feedback between one or more internal state variables and their terminal current and/or voltage.[17] When such a framework applies, the device so described is a memristive system, or more simply, a memristor.[18] A memristor compact model consists of: 1) an electrical conductance function that depends on at least one state variable x, and possibly, either current i or voltage v, together with 2) a state equation that links the dynamical evolution dx/dt to x and i and/or v.

For transition metal oxides like TiO_x and NbO_2, good agreement with experiment has been obtained using a 1D generic electro-thermal compact model for which there is a single temperature state variable governed by Newton's law of cooling dynamics.

Hence, the assumed compact model for VO_2 studied here is also of the form

$$i = G_{el}(T)v \tag{2a}$$

$$\frac{dT}{dt} = \frac{1}{C_{th}(T)}\left(iv - G_{th}(T)(T - T_0)\right) \tag{2b}$$

where T is the internal memristor temperature, T_0 is the ambient temperature, the G's are electrical or thermal

conductance functions with units (A V^{-1}) or (W K^{-1}) and notated by subscript "el" or "th", respectively, and $C_{th}(T)$ is the thermal capacitance function (heat capacity) in (JK^{-1}).

A successful characterization of a memristor from this perspective requires in principle a complete determination of the temperature-dependent functions ($G_{el}(T)$,$G_{th}(T)$,$C_{th}(T)$) from experimental data. Additionally, we desire that the compact model should be material-dependent as opposed to device-dependent, in the sense that the temperature-dependent conductance and capacitance functions should be known in terms of purely material parameters, such as activation energies, specific heats, and conductivities, with any dimensional dependence accounted for separately with appropriate pre-factors, e.g., $G_{el} = (LW/H)\ \sigma$. Such models should ideally transfer between different memristor devices according to scaling laws, and therefore, characterize the component material of the memristor, as opposed to incidental devices with particular dimensions.

At steady-state ($dT/dt = 0$), the temperature T and DC current I and voltage V are mutually interdependent, expressed as

$$G_{el}(T)V^2 = \frac{I^2}{G_{el}(T)} = G_{th}(T)(T - T_0) \tag{3a}$$

$$I = G_{el}(T)V \tag{3b}$$

Practically, this means that on the steady-state curve only one of the three variables (I,V,T) is free, and automatically determines the other two. This mutual dependence is useful, since typical I–V characterization is performed by setting a control DC current or voltage, which in turn sets a corresponding bias temperature T, and then averaging the resultant voltage or current over time, which, for long averaging and wait times, should closely approximate the steady-state curve. In what follows, the temperature perspective is most useful, and we will define and analyze several bias-dependent quantities as functions of T.

The compact model (Equations (2a) and (2b)) admits computationally useful behaviors, such as NDR on the steady-state curve (Equations (3a) and (3b)), or self-oscillation, when the electro-thermal conductance is nonlinear. In turn, nonlinearity enables local activity (i.e., the capability for utilizing DC power to amplify energy fluctuations), as distinct from local passivity (i.e., the impossibility of utilizing DC power to amplify energy fluctuations). The state of local activity (LA) versus local passivity (LP) is related but independent from local stability; an LP state is locally stable and can never be destabilized but an LA state can be stable or unstable. The special condition of a device being both LA and locally stable is defined as Edge of Chaos (EOC). EOC designates the unique variety of stability that can be destabilized by external coupling, thereby leading to useful dynamics. In contrast, the set difference of LA and EOC, notated LA\EOC, are inherently unstable and cannot be stabilized. Hence, nonlinearity underpins all of these phenomena and is a major factor in desired dynamical behavior.

We find that a useful metric of nonlinearity linking the electro-thermal memristor model at a given bias T to NDR, local activity/passivity, and EOC is the pair of unitless nonlinearity parameters,[5a,19]

$$\Gamma_{\pm}(T) \equiv \left(\frac{G_{el}'(T)}{G_{el}(T)} \pm \frac{G_{th}'(T)}{G_{th}(T)}\right)(T - T_0) \pm 1 \tag{4}$$

where superscript primes denote temperature derivatives. There is a one-to-one relationship between the $\Gamma_{\pm}$ nonlinearity parameters determined by the electro-thermal conductances and the LP/LA condition of a particular region of the device I–V curve:

- **If** $\Gamma_+ > 0$
  - **If** $\Gamma_- < 0$: LP
  - **If** $\Gamma_- > 0$: EOC
- **Otherwise**: LA\EOC

The nonlinearity parameters (Equation (4)) relate to analyses that determine both EOC and NDR, such that for the preponderance of compact models, NDR on the steady-state curve is an equivalent manifestation of the dynamical property of EOC. For example, for oxides that become more electrically conductive at higher temperature ($G_{el}'(T) > 0$), both local activity and NDR occur only at bias temperatures T for which $\Gamma_-(T) > 0$. The existence of two nonlinearity parameters accounts for the mutual independence of local activity and local stability. For example, EOC additionally requires $\Gamma_+(T) > 0$.[5a] There is therefore a delicate balance in creating large enough electro-thermal nonlinearities to enable EOC -NDR, but not so large as to totally destabilize the steady state of interest.

The 1D generic electro-thermal compact model (Equations (2a) and (2b)), like all 1D dynamical systems, is by itself incapable of either transient or persistent oscillations, since oscillations are possible only in dynamical systems with two or more state variables.[20] Nonetheless, in this work and others, continuous self-oscillations in a region of NDR are experimentally observed. Hence, the 1D electro-thermal memristor model considered in isolation is insufficient to account for the dynamical phenomena. The solution is that there is no such thing as a "pure" physical memristor obeying only Equations (2a) and (2b). Instead, every physical device and every characterization experiment is a compound network of nodes described mathematically by model circuit elements, and every experiment consists of a network one wishes to characterize, together with external circuitry providing and measuring electrical signals.

In the present case, the lateral VO_2 devices exhibit not only electro-thermal nonlinear physics modeled by memristor behavior, but also a metal–insulator–metal structure that contributes some electrical capacitance. Furthermore, dynamical devices have primarily been characterized using commercial black box source-measure units designed for repeatable, high-accuracy measurements of passive devices, but which come at the expense of complicated and proprietary circuitry with undocumented impedances. Regardless of the origin, there is certainly some capacitance C_{eff} in the source or device (Figure 1b), which in turn supports a second state variable, equivalently, charge or capacitor voltage, with its own dynamics described by

$$\frac{dv}{dt} = \frac{1}{C_{eff}}\left(I - G_{el}(T)v\right) \tag{5}$$

Together with Equations (2a) and (2b), Equation (5) constitutes one part of a coupled system of two first-order nonlinear differential equations.

For passive devices,[8a] the coupling between the temperature and voltage state variables can lead only to transient oscillations that decay into a stable steady state. However, for locally active devices,[8a] the coupled thermal and electrical dynamics may produce self-oscillations persisting through all time from a DC bias provided that a) the DC bias is EOC and b) the destabilizing electrical device capacitance is large enough. By linearizing the nonlinear system Equations (1a), (1b), and (4), it can be shown using Laplace methods that the destabilizing capacitance must be greater than a critical value,[5a] given by $C_{\text{eff}} > C_{\text{eff}}^{\text{crit}}(T)$ with

$$C_{\text{eff}}^{\text{crit}}(T) = C_{\text{th}}(T)\left(\frac{G_{\text{el}}(T)}{G_{\text{th}}(T)}\right)\frac{1}{\Gamma_{-}(T)} \tag{6}$$

Equation (6) shows that $C_{\text{eff}}^{\text{crit}}(T)$ is thus dependent on the bias temperature, the electrical and thermal conductances, the thermal capacitance, and the nonlinearity parameter $\Gamma_{-}(T)$ at that bias. The necessary condition of EOC is built into Equation (6), i.e., a physical critical capacitance $C_{\text{eff}}^{\text{crit}} > 0$ is only possible if the bias state is EOC, $\Gamma_{-}(T) > 0$.

The presence or absence of persistent self-oscillations is jointly dependent on the compact model, the nonlinearity parameters of the memristor core, and the effective device capacitance. Hence, elements that are external to the memristor core of the device must also be incorporated into the compact model. A particularly useful characteristic is the dependence of the self-oscillation frequency on the nonlinearity parameters, and on the critical and actual device capacitances at a particular NDR-EOC bias temperature T. Using the same linear/Laplace methods,[5a] the frequency dependence (Equations (7a) and (7b)) in terms of a normalized capacitance $c \equiv C_{\text{eff}} / C_{\text{eff}}^{\text{crit}}$ is

$$\left(\frac{f}{f_0}\right)^2 = 4\frac{\Gamma_{+}}{\Gamma_{-}}\left(\frac{1}{c}\right) - \left(1 - \frac{1}{c}\right)^2 \tag{7a}$$

where

$$f_0(T) \equiv \frac{1}{4\pi}\left(\frac{G_{\text{th}}(T)}{C_{\text{th}}(T)}\right)\Gamma_{-}(T) \tag{7b}$$

is a convenient frequency (s^{-1}) pre-factor.

Note that all of Equations (2)–(7) are written in terms of a non-specific electrical conductance $G_{\text{el}}(T)$ and thermal conductance $G_{\text{th}}(T)$. In other words, the dynamical properties of electro-thermal memristors as specified by the local activity theory depend directly on the temperature dependence of the electro-thermal transport but on nothing more fundamental, e.g., energy barriers or particular transport physics. The fundamental physics governing the dynamical properties, which is Newton's Law of Cooling, is agnostic with respect to what transport physics or intrinsic materials properties underly electro-thermal transport, and therefore, the dynamical properties are similarly agnostic. The only criterion is that the resultant functions $G_{\text{el}}(T)$ and $G_{\text{th}}(T)$ are sufficiently nonlinear, according to Equation (4). In the present work, these facts guarantee that the collected data can be inverted to directly characterize the nonlinear electro-thermal properties of VO_2/SiN devices, leaving the physical mechanisms underlying this transport to necessary future work.

By exploiting the quantitative links between steady-state and dynamic behavior and the required compact model parameters ($G_{\text{el}}(T), G_{\text{th}}(T), C_{\text{th}}(T)$) embodied by Equations (2)–(7), we developed a systematic fitting procedure to determine a set of material-dependent model parameters with low uncertainty and high predictive power. We first used Equations (3a) and (3b) to fit the measured quasistatic I–V–T behavior of all the devices and determined the electro-thermal conductances $G_{\text{el}}(T)$ and $G_{\text{th}}(T)$ in terms of material-dependent parameters ($\alpha, \sigma(T), \kappa(T)$). Then we used Equations (4), (6), (7a), and (7b) to fit the measured T-dependent self-oscillation frequencies f throughout the Edge of Chaos NDR region of one device to determine the fixed but unknown external electrical capacitance C_{eff}, and the thermal capacitance $C_{\text{th}}(T)$ in terms of material-dependent specific heat ($c_{\text{th}}(T)$). Each of these steps was performed with least-squares based optimization routines, meaning that the fitting procedure was fast, systematic, and provided reasonable estimates of uncertainty from the data. Finally, we numerically simulated the nonlinear system Equations (2a), (2b), and (5) to generate modeled electro-thermal oscillations for comparison with experimental data.

Finally, as a caveat, Equations (7a) and (7b) were derived from linearizations of the compact model (Equations (2), (3), and (5)) and are only approximations to the nonlinear circuit. However, we have found that the linear equations provide an excellent approximation to the frequencies determined by numerical simulation of the full compact model. Thus, fitting experimental data to the linearization approximations Equations (6), (7a), and (7b) was an excellent starting point for later parameter fine-tuning.

3.2. Physically Motivated Modeling Assumptions

Characterizing quasistatic I–V curves for devices with varying device dimension (Figure 3) set the stage for determining the desired compact model parameters wholly in terms of measurable material properties. This task would be relatively simple if the current, voltage, and temperature were all measured independently within both the intra- and extra-channel volumes. In this case, the steady-state curve Equations (3a) and (3b) could be fit in steps, first fitting the unknown $G_{\text{el}}(T)$ using the equivalent formulation,

$$G_{\text{el}}(T) = \frac{I(T)}{V(T)} \tag{8a}$$

then fitting the unknown $G_{\text{th}}(T)$ with

$$G_{\text{th}}(T) = \frac{I(T)V(T)}{T - T_0} \tag{8b}$$

according to reasonable physically motivated models for $G_{\text{el}}(T)$ and $G_{\text{th}}(T)$.

However, despite a fairly complete electrical and thermal characterization, there are two difficulties. First, the *I*–*V* characterization is only capable of measuring the net current and voltage applied to the entire device volume. Second, since the temperature response of the thermoreflectance technique was limited to near the window of the IMT, temperature data were only available within the hot channel. In order to use Equations (8a) and (8b) with the data, it was necessary to both compute a reasonable partition of the net current and voltage between the intra- and extra-channel volumes, and also to independently compute a reasonable estimate for the unmeasured temperature of the extra-channel volume.

In order to develop this partition, we made several assumptions:

i) The channel first appears at the onset of the NDR regime of the quasistatic *I*–*V* curve.
ii) The channel extends vertically through the whole thickness *H* of the device; therefore, the partition between volumes is equal to the partition in terms of area.
iii) The formation of the channel area does not significantly affect the transport of the extra-channel area.
iv) The thermal coupling of the intra- and extra-channel areas with each other is negligible compared to the thermal coupling of each with the substrate.
v) The electrical and thermal conductance are weak functions of temperature well below the FOPT.

These assumptions are supported theoretically on physical grounds and indirectly by the experimental data. For example, (i) Ridley predicted that entropy generation favors steady-state localized current when the sign of dV/dI is negative,[15] i.e., in a regime of NDR. Assumption (ii) is motivated by the fact that the devices have only 100 nm thickness, and from the optical physics underlying thermo-reflectance, the signal should be volume-sensitive, not surface-sensitive. Assumption (iii) follows from the continued observation of a hot channel in a cool device after the FOPT discontinuity (Figure 5a, 3.56 mA → 3.40 mA data), showing that a sudden change in channel morphology does not create a second channel or otherwise affect extra-channel transport. Assumption (iv) is supported by the observation of only single frequency oscillations in the NDR regime; whereas if the intra- and extra- channel areas were thermally coupled, there should be at least two frequencies beating against each other. Dimensional analyses also favor (iv): assuming worst-case that the effective thermal conductance from hot VO_2 to cool VO_2 is 5 × that from VO_2 to the SiN substrate, and that $T - T_0$ for the extra-channel area is half that of the intra-channel area, the typical interfacial areas imply that the heat loss to the substrate is still 88% and 75% for the intra- and extra-channel volumes, respectively. Finally, assumption (v) follows from the initial resistivity–temperature characterization (Figure 2a).

4. Compact Model Fitting

4.1. Electrical and Thermal Conductance Before NDR Onset

The electrical conductance of VO_2 is in general, highly nonlinear, especially around the IMT. However, based on the data and modeling assumptions (i) and (v), we postulated that the device conductance in the PDR region well below the FOPT was uniform (no channel), and that the electrical and thermal conductance functions were approximately linear and constant, respectively, i.e.,

$$G_{\mathrm{el}}\left(T < T_{\mathrm{NDR}}\right) = G_{\mathrm{el}}\left(T_0\right)\left(1 + \alpha\left(T - T_0\right)\right) \tag{9a}$$

$$G_{\mathrm{th}}\left(T < T_{\mathrm{NDR}}\right) = G_{\mathrm{th}}\left(T_0\right) \tag{9b}$$

where $\alpha > 0$ (K^{-1}) is the increase in the electrical conductance, as a fraction of the baseline value $G_{\mathrm{el}}(T_0)$. For uniform conductance, dimensional scaling laws apply, i.e., the thermal conductance increases with interfacial area, and the electrical conductance increases with area normal to current flow and decreases inversely as the length parallel to current flow. In terms of the device dimensions (L,W,H),

$$G_{\mathrm{el}}\left(T_0\right) = \sigma_0 \frac{WH}{L} \tag{10a}$$

$$G_{\mathrm{th}}\left(T_0\right) = \kappa_0 LW \tag{10b}$$

where $\sigma_0 = \sigma(T_0)$ is the baseline electrical conductivity (Sm^{-1}) and $\kappa_0 = \kappa(T_0)$ is the effective baseline interfacial thermal conductivity ($W\,K^{-1}\,m^{-2}$).

The steady-state curve Equation (3) can be combined with the assumed linear functional form Equations (9a) and (9b), and with the scaling laws Equations (10a) and (10b). We then solved for current in terms of voltage, leading to

$$I\left(V,L,W,H;\sigma_0,\alpha/\kappa_0\right) = \frac{V}{\left(\frac{L}{WH}\right)\left(\sigma_0\right)^{-1} - \left(LW\right)^{-1}\left(\frac{\alpha}{\kappa_0}\right)V^2} \tag{11}$$

The *I*–*V* characteristic Equation (11) constitutes a measured output *I*, in terms of a known input *V*, three known fixed dimensional parameters (L,W,H), and two unknown material parameters ($\sigma_0,\alpha/\kappa_0$), and is amenable to nonlinear least-squares optimization. Fitting the quasistatic *I*–*V* curves below the NDR region for all devices with varying dimension (**Figure 6**) using the Matlab lsqcurvefit function yielded

$\sigma_0 = (1.581 \pm 0.011) \times 10^{-3}$ [S μm^{-1}], and
$\alpha/\kappa_0 = (1.73 \pm 0.11) \times 10^{3}$ [μm^2 W^{-1}].

The uncertainties are 95% confidence intervals using the approximated Jacobian of the lsqcurvefit optimizer. The standard error of regression (SER), which is the average absolute deviation between all predicted and actual voltages, was 0.05 mA, or 3–5% of a typical full-scale range of 1–1.5 mA. Despite the relatively small overall regression error, it appears that some subsets of the devices, particularly the constant-width, varied-length subset, have a larger error than the mean. This is likely due to slight compositional variation: cross-chip resistivity–temperature plots (Figure S2, Supporting Information) demonstrate that devices from different areas on the chip can vary by about a factor of two, and due to the device structure the devices with constant-width, varied length comprise a larger area of the chip. Imperfectly defined lithographic device dimensions may also

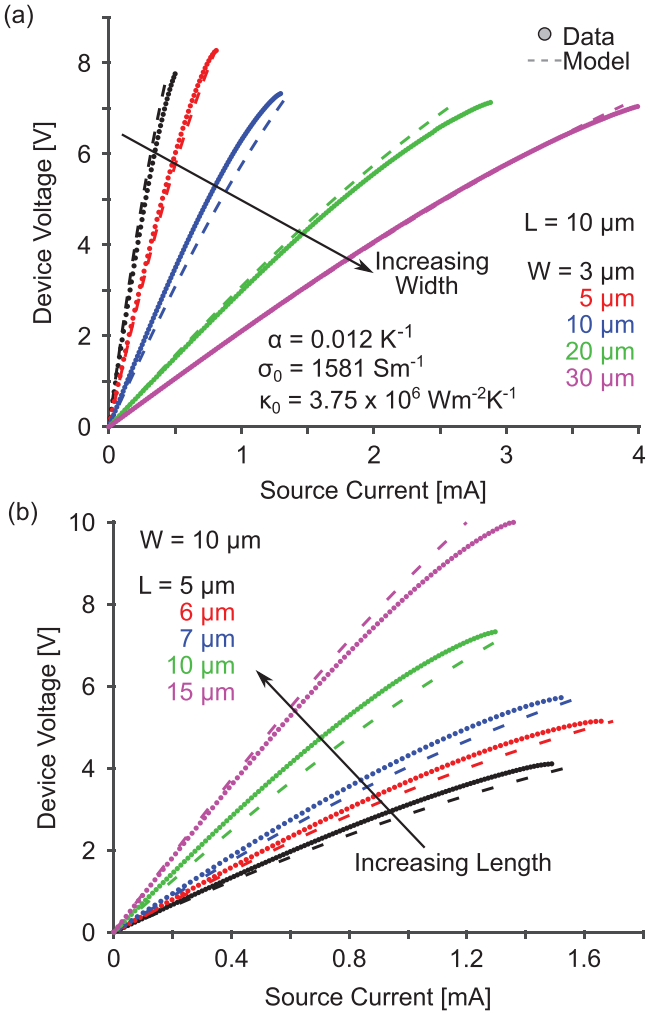

Figure 6. Self-consistent electro-thermal compact model (Equations (9)–(11)) fit simultaneously to all quasistatic *I–V* data up to the occurrence of NDR. a) Data and fitted compact model for devices with 10 μm length and varying width. b) Data and fitted compact model for devices with 10 μm width and varying length. Uncertainties in data (manufacturer specification) are 3 mV, 0.1 μA.

play into the model error. Nevertheless, despite these individual factors, the overall variance in conductance is dominated by scaling laws like Equations (10a) and (10b), strongly suggesting uniform conduction in this region.

Although the linearized model Equations (9)–(11) are fully described by the parameters $(\sigma_0, \alpha/\kappa_0)$, additional physical insight is gained by determining the three physical parameters $(\sigma_0, \alpha, \kappa_0)$ separately. In order to separate the individual parameters (α, κ_0) from their ratio, we determined that the onset NDR temperature corresponding to the peak *I–V* point just before channel formation was 330 ± 2 K. This temperature is below the window of the thermoreflectance technique and was determined by other means (Figures S5 and S6, Supporting Information).

Combining Equation (3) with Equations (10a) and (10b) yields

$$T = T_0 + I(T)V(T)/\kappa_0 LW \tag{12}$$

in which only κ_0 is unknown. From the (L, W) = (8 μm, 10 μm) *I–V–T* data (Figures 3 and 4), we estimated

$\kappa_0 = (3.75 \pm 0.16) \times 10^{-6}$ [W μm^{-2} K^{-1}],
$\alpha = 0.0123 \pm 0.0005$ [K^{-1}].

The parameter α is of the order of 0.01 K^{-1}, which is consistent with modeling assumption (v) of a small, linear dependence of the electrical conductance on temperature within the initial PDR region, Equation (9a). Together with Equations (3), (9), and (10), and the three fitted parameters $(\alpha, \sigma_0, \kappa_0)$, Equation (12) supplied the complete quasistatic *I–V–T* characterization of the VO_2 active material below the NDR onset.

4.2. Electrical and Thermal Conductance Within and After NDR

According to the assumptions of Section 3.2, we modeled each of the intra- and extra-channel device volumes as a thermal memristor with internal temperature *T* (**Figure 7**a). Since the intra-channel and extra-channel volumes were electrically in parallel, the current and voltage contributions of the intra- and extra-channel areas to the total *I–V* curve were partitioned as (Figure 7b):

$$V_0 = V_1 = V_2 \tag{13a}$$

$$I_0 = I_1 + I_2 \tag{13b}$$

with subscript "0" the measured net device current/voltage, "1" the modeled extra-channel current/voltage determined by the $(\alpha, \sigma_0, \kappa_0)$ compact model, and "2" the intra-channel current/voltage contribution. According to assumptions (iii) and (iv), the extra-channel memristor continued to be well-described by the compact model of Equations (9)–(12) within the net device's NDR region, with the same $(\alpha, \sigma_0, \kappa_0)$ as in the PDR region. Only the extra-channel and intra-channel widths change (Figure 4c), respectively, from

Extra-channel: $w \rightarrow w - w_{\text{chan}}$
Intra-channel: $0 \rightarrow w_{\text{chan}}$

Thus, (I_1, V_1, T_1) was determined from the compact model of the PDR region, and (I_2, V_2) was deduced from the net device data and parallel decomposition Equations (13a) and (13b). Finally, T_2 was independently measured by the thermoreflectance characterization.

We have visualized both the intra-/extra-channel *I–V–T* contributions in **Figure 8** together with a uniform conduction model computed using the measured *I–V* data in direct combination with the linear compact model from Section 4.1. The three *I–V–T* curves together describe the decomposition of a theoretical lumped device with constant properties (i.e., current density and temperature) into two independent volumes, each with their own different characteristic properties. The fact that the current density and temperature of the uniform model were between those of the intra- and extra-channel volumes is self-consistent with modeling assumption (i) of a uniformly conducting volume spontaneously decomposing into a hot channel and cool exterior. This is analogous to the

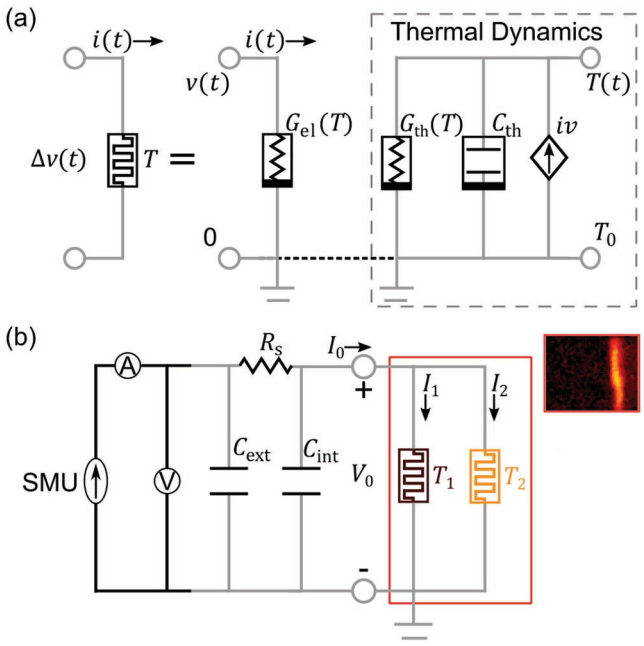

Figure 7. Circuit schematics for bipartite parallel memristor decomposition. a) Electro-thermal memristor with internal temperature T represented as a state-dependent nonlinear conductor $G_{el}(T)$ coupled to a nonlinear thermal-equivalent circuit representing the dynamics of Equation (2b). b) Circuit schematic of the device-and-characterization network representing the partition of the total device area (Equations (13a) and (13b)) into two parallel memristors with independent temperatures T_1 and T_2.

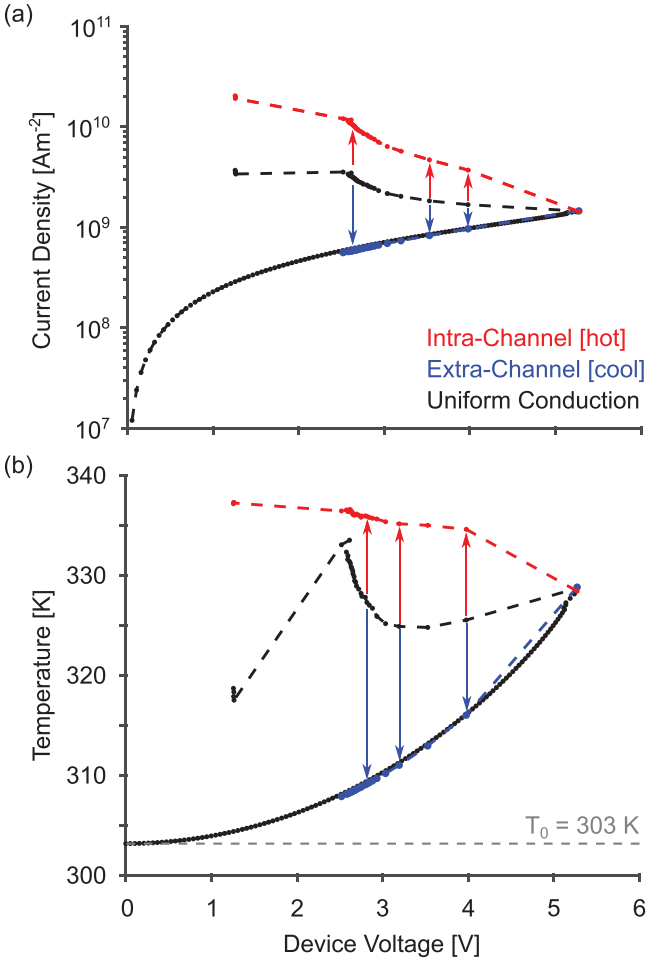

Figure 8. Decomposition of intra- and extra-channel area contributions for the device ($L = 8$ µm, $W = 10$ µm) to quasistatic current density, voltage, and temperature, according to the parallel memristor model Equations (13a) and (13b). a) Current density on a log scale versus bias voltage for the intra- and extra-channel areas, as well as values calculated for a fictitious lumped device. Uncertainties are less than 15 µA, 20 mV, as in Figure 4a. b) Similar decomposition plot for the quasistatic temperature versus bias voltage. Uncertainties are less than 15 µA, 0.06 K, as in Figure 5b.

decomposition of a metastable, homogeneous chemical phase into multiple individual phases with their own individual composition, and suggests a deep but not yet totally understood connection between decomposition of thermodynamic properties at equilibrium and decomposition of other physical quantities at steady-state. Furthermore, the uniform conduction model resulted in the steady-state temperature decreasing for some points in the NDR region despite increased current density and power dissipation; whereas, for both the intra-channel and extra-channel models, the temperature always increased with increased current density and power dissipation. Although not strictly impossible, the first case is improbable compared to the second. Hence, the bipartite decomposition is a necessary step to ensure the probable intuition that within each volume of the partition, the temperature increases monotonically with the Joule power dissipation.

From the decomposed and measured (I_2, V_2, T_2) and Equations (8a) and (8b) (embodying assumption (iv)), the electrical conductivity $\sigma(T)$ and area-normalized interfacial thermal conductivity $\kappa(T)$ for temperatures within the NDR region were reconstructed (**Figure 9**). An identical analysis, including thermal mapping, I–V decomposition, and steady-state computations, was also performed for a device with (L = 15 µm, W = 10 µm) dimensions, and combined with the (L = 8 µm, W = 10 µm) data to extend the data to higher temperatures (Figure 9, red markers).

For the electrical conductivity, there are two potential sources of data: the direct isothermal measurements in Figure 2a and the steady state data computed through the decomposition in Figures 7 and 8. In creating the electro-thermal compact model (Figure 9a), we chose to prioritize the data source with fewer complications and greater data density, and so fit the model to the iso-thermal data. The logarithm of the electrical conductivity modeled thus is well represented by two linear functions L_1 and L_2, interpolated by a sigmoidal function $u(T)$:

$$\log_{10}\sigma(T) = L_1(T)\big(1-u(T)\big) + L_2(T)u(T) \tag{14a}$$

$$L_{1,2}(T) = b_{1,2} + m_{1,2}\left(\frac{T}{300\ \mathrm{K}} - 1\right) \tag{14b}$$

$$u(T) = \frac{1}{2} + \frac{1}{2}\mathrm{erf}\left(1.72\frac{T-T_c}{\delta T}\right) \tag{14c}$$

where erf is the error function, defined as the indefinite integral of the standard normal function, T_c is the critical temperature

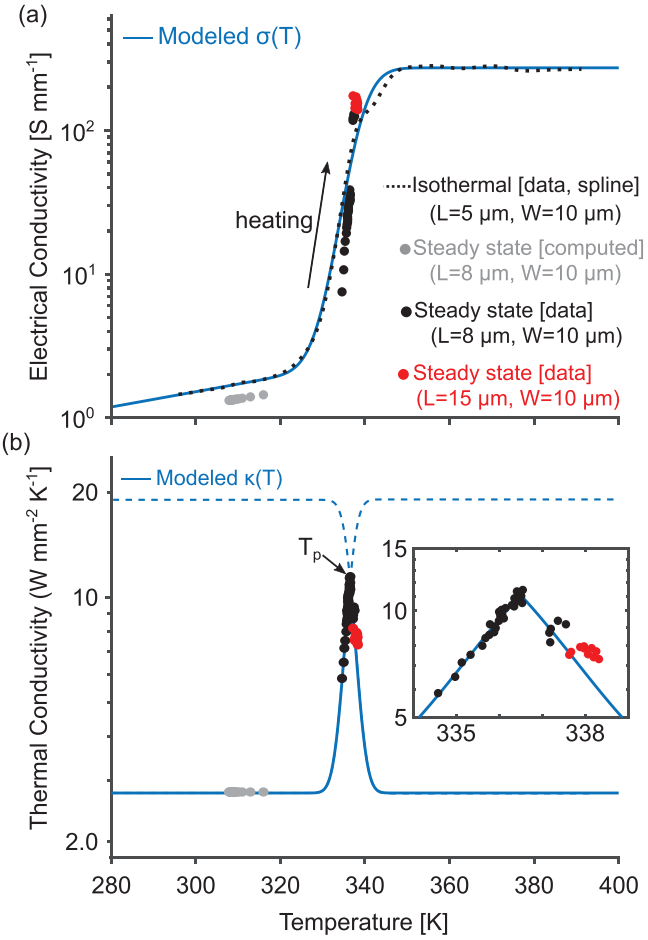

Figure 9. Fitted models for electrical and thermal conductivities. a) Electrical conductivity (log scale) (Table 2), developed from steady-state data from multiple devices and isothermal data from Figure 2a. Uncertainties (propagated from *I*,*V*) are less than 0.5 S mm^{-1} b) Thermal conductivity (log scale) (Table 3) developed from steady-state data measured on two independent devices. The model was developed by constraining a sigmoid (dashed line) to be symmetric about the peak temperature T_p (black arrow). Inset: Enlarged view of data and model near the peak. Uncertainties (propagated from *I*,*V*,*T*) are less than 0.2 W mm^{-2} K^{-1}.

where the unit step $u(T)$ reaches 50% completion. The prefactor 1.72 within the erf argument ensures that δT is properly scaled as the temperature interval between which $u(T)$ changes from 10% to 90% completion. The model (Equations (14a), (14b), and (14c)) parameters and uncertainties for $\sigma(T)$ are displayed in **Table 2**.

The general agreement between the steady-state data and isothermal data obtained for two independent devices is an important observation itself. For isothermal measurement, the temperature was controlled independently, the device conduction was uniform, and the *I*–*V* sweep was at relatively low power (≤50 mV); whereas for steady state, the temperature was dependently constrained by Newton's law of cooling, the device conduction was non-uniform, and the voltages were orders of magnitude higher (1–10 V). Despite this, there is qualitative agreement between the methods, with a maximum difference of 92 S mm^{-1} near the inflection point of the transformation. From a practical point of view, the isothermal measurement

Table 2. Compact model parameters for temperature-dependent electrical conductivity, $\sigma(T)$, Equations (14a), (14b), and (14c). Uncertainties were calculated from the estimate of the Jacobian matrix from the MATLAB nlinfit function. Units of $b_{1,2}$ are such that $10^{b_{1,2}}$ has units of conductivity, S m^{-1}.

Electrical Conductivity, $\sigma(T)$			
Parameter	Units	Fitted Value	Uncertainty
b_1	$\log_{10}$ [S m^{-1}]	3.1801	±0.0034
b_2	$\log_{10}$ [S m^{-1}]	5.43	±0.01
m_1	[1]	1.60	±0.14
m_2	[1]	0	–
T_c	[K]	334.2	±0.2
δT	[K]	17.4	±1.2

was much easier than the steady-state characterization, and so the former can be performed and used to supplement a relatively small steady-state data set provided that: 1) the source power during isothermal measurement is kept low enough to prevent self-heating, and 2) the steady-state *I*–*V* data is properly decomposed between the intra- and extra-channel areas.

In contrast, the interfacial thermal conductivity $\kappa(T)$ has some features of a sigmoid, but also has a cusp-like peak near T_p = 336.5 K. This result is surprising, but also resolves two seemingly contradictory observations. First, there is a clear and well-documented increase in the electrical conductivity of VO_2 near the martensitic transition; since this is believed to result from a sudden increase of carriers in the conduction band, we should expect these carriers to simultaneously contribute to an increased thermal conductance, by the Wiedemann–Franz law. Second, the apparent hysteresis in the quasi-DC *I*–*V* curve is a signature of globally unstable, locally active PDR, which, if $G_{el}(T)$ is monotonically increasing, requires from Equation (4) that $G_{th}(T)$ must sharply decrease within the temperature interval corresponding to the hysteresis. The resolution to this apparent inconsistency supported by the data is that the thermal conductivity does both: it first increases sharply along with the electrical conductivity, then sharply decreases even as the electrical conductivity continues to increase. This latter regime implies that some other factor negates and dominates the contribution of the increased carrier concentration near the Mott transition. Recent work has demonstrated qualitatively similar non-monotonic thermal behavior termed negative differential thermal conductivity in a variety of systems, attributed to temperature-dependent negative thermal expansion in bulk Si homojunctions, or electron–phonon scattering across a metal–dielectric interface.[21] This opens the intriguing possibility for future investigation that the non-monotonic thermal conductivity in VO_2—and its consequent locally active PDR—may be caused by, and may potentially be engineered by, the changing phonon transport across the VO_2-substrate interface as the temperature approaches the MIT.

Continuing with the model, when $T \leq T_p$, the dependence is substantially sigmoidal and we fit it similarly as for $\sigma(T)$. For $T > T_p$ the data is sparse even after combining data sets for different devices, since the rate of heating for a given increase of current slows down dramatically as the thermal conductivity suddenly decreases. The combined data after T_p is sufficient to

Table 3. Compact model parameters for temperature-dependent interfacial thermal conductivity, $\kappa(T)$. Uncertainty for T_p is taken from the half-width of the peak at 90% peak maximum. All other uncertainties are computed from estimated Jacobians from the MATLAB nlinfit optimizer.

Interfacial Thermal Conductivity, $\kappa(T)$			
Parameter	Units	Fitted Value	Uncertainty
c_1	$\log_{10}$ [W m^{-2} K^{-1}]	6.44	±0.16
c_2	$\log_{10}$ [W m^{-2} K^{-1}]	7.28	±0.22
T_c	[K]	335.2	±0.6
δT	[K]	7.2	±2.0
T_p	[K]	336.5	±0.5

establish the presence of a cusp-like peak, but not enough to provide a quantitative functional form for $T > T_p$. However, the data suggest that the peak is symmetric about T_p, and a simple extrapolation under a lack of additional data is that $\kappa(T)$ for $T \gg T_p$ is symmetric about T_p.

Other extrapolation methods for $T > T_p$ were attempted but each had significant limitations. For example, a linear extrapolation eventually yields unphysical negative values for $\kappa(T)$ and a $1/T$ reciprocal extrapolation is poorly matched to the sparse data. A last attempt to fit the data using a product of sigmoids, as in $u(T) \times (1 - u(T))$ did not totally capture the inherent cusp-like shape of the peak suggested by the data (Figure S7, Supporting Information). In contrast, the T_p-symmetric extrapolation fits the cusp-like peak well, introduces no extra parameters, and extrapolates to high temperatures without $\kappa(T)$ ever becoming negative or unbounded, and so we used a model of the form:

$$\log_{10}\kappa(T) = c_1\left(1 - U(T)\right) + c_2 U(T) \tag{15a}$$

$$U(T) = \frac{1}{2} + \frac{1}{2}\mathrm{erf}\left(1.72\frac{T - T_c}{\delta T}\right),\ T \le T_p \tag{15b}$$

$$U(T) = \frac{1}{2} + \frac{1}{2}\mathrm{erf}\left(1.72\frac{2T_p - (T + T_c)}{\delta T}\right),\ T > T_p \tag{15c}$$

Here $U(T)$ is analogous to the previous sigmoid $u(T)$, but defined piecewise to be symmetric about T_p. The result is the union of the lower branches of two $u(T)$ sigmoids with the same height, center, and width, reflected through $T = T_p$ (Figure 9b). The model (Equations (15a), (15b), and (15c)) parameters and uncertainties for $\kappa(T)$ are displayed in **Table 3**.

4.3. Nonlinearity Parameters, Local Activity, and NDR

The nonlinearity parameters (Equation (4)) provide the key to quantifying local activity and NDR, and also to modeling self-oscillations as in Equations (7a) and (7b). Since the dimensional device factors (L, W, H) in the terms G_{el}'/G_{el} and G_{th}'/G_{th} appear in both numerator and denominator and cancel, the nonlinearity parameters can be further simplified to

$$\Gamma_{\pm}(T) \equiv \left(\frac{\sigma'(T)}{\sigma(T)} \pm \frac{\kappa'(T)}{\kappa(T)}\right)(T - T_0) \pm 1 \tag{16}$$

Equation (16) provides a direct link from the electro-thermal conductivities modeled in Section 4.2 to local activity, NDR, and oscillation frequencies.

In the language of local activity theory, the PDR region on the I–V curves through the origin is Locally Passive (LP); it is inherently stable and therefore accessible to both current and voltage sweeps, and cannot lead to instability or oscillations. The NDR region is EOC, and it is stable but capable of destabilization, resulting in it being stable with respect to current sweeps but unstable with respect to voltage sweeps. The capability of the NDR region as a locus of stable steady states to be destabilized by external capacitive coupling is what enables self-oscillations, which similarly signify local instability and global stability. Finally, the hysteresis feature contains an interior region that is both locally and globally unstable LA\EOC, and therefore, inaccessible to both current and voltage sweeps. In this respect, each device passes through the sequence {LP, EOC, LA\EOC, LP} as it self-heats along the quasistatic I–V curve.

The electro-thermal conductivity model constructed in Section 4.2 must at least be consistent with the experimentally observed sequence {LP, EOC, LA\EOC, LP} corresponding to PDR, NDR, hysteresis, PDR. To demonstrate this, we first calculated the derivatives (**Figure 10**a, inset) σ'/σ and κ'/κ from the model Equations (14) and (15), followed by the nonlinearity parameters Equation (16) (Figure 10a). The plot shows that the effect of the thermal conductivity having a sharp peak is to cause its derivative to be negative directly after the peak, which in turn, causes the nonlinearity parameter Γ_+ to also be negative.

Thus, the peak in the thermal conductivity is the source of the LA\EOC region that lies within the interior of the hysteresis feature on the I–V curves.

Simultaneously, we have computed the corresponding steady-state curve (Figure 10b, compare Figure 2b) as functions of T using Equation (3), written in the form

$$(I, V) = \left(\sqrt{G_{el}(T)G_{th}(T)(T - T_0)}, \sqrt{\frac{G_{th}(T)(T - T_0)}{G_{el}(T)}}\right) \tag{17}$$

The plots of the nonlinearity parameters and steady-state curve (Equation (17)) derived from the model are generally consistent with expectations. There is initially a large region of LP/PDR, followed by a substantial region of EOC / NDR capable of self-oscillations. Then there is a second region of LP/PDR, but the positive slope of this region is small. Following this is the only region of LA\EOC resulting from the sharply decreasing thermal conductivity, and it is clear from the steady-state curves that this is also a region of PDR ($dV/dI > 0$). This is Locally Active PDR, and exists only within the interior of the hysteresis loop, which is inaccessible to current or voltage sweeps by virtue of its inherent instability. Importantly, within this region both current and voltage decrease as the temperature increases (Figure 10c), so that the channel temperature at the upper-right of the LA-PDR region (point A) is *lower* than the temperature at the lower-left of this region (point B), despite the current and voltage being higher. Hence, the discontinuous decrease in voltage and current displayed in Figure 4a, and the corresponding increase in temperature displayed in Figure 5b,

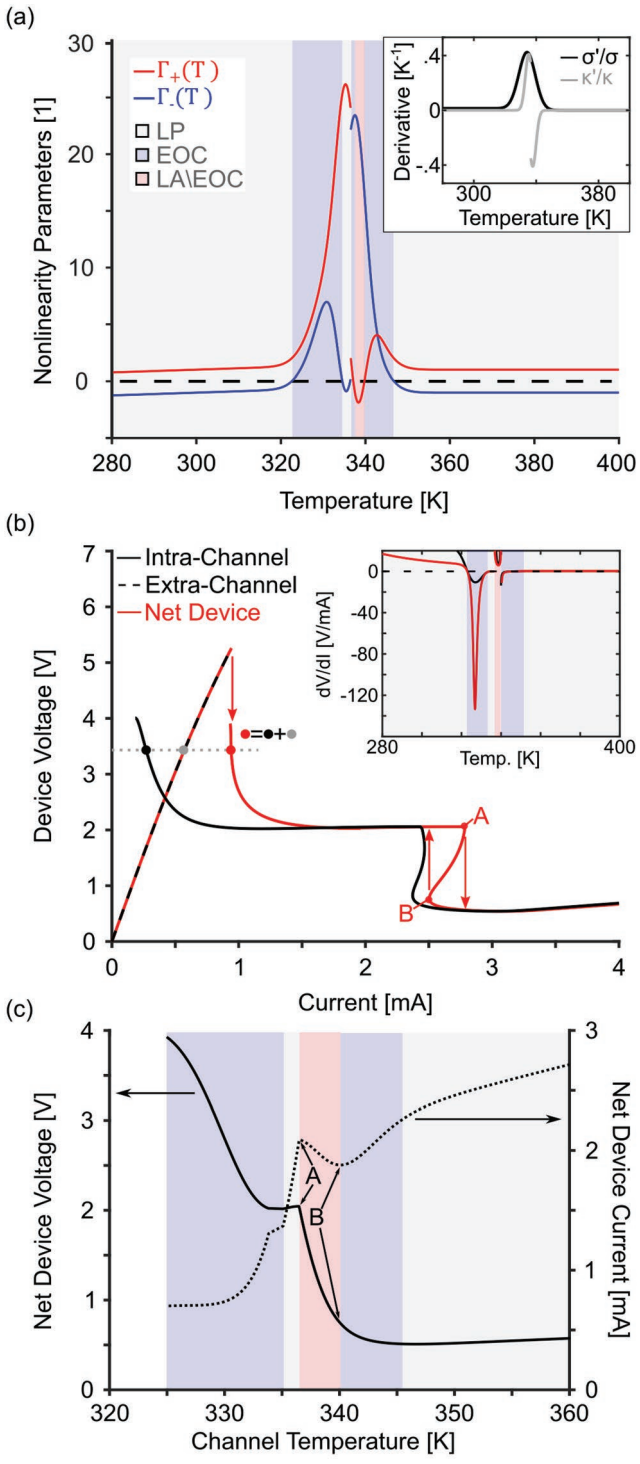

Figure 10. Relationship between steady-state features, local activity, and electro-thermal conductivities. a) The interaction between the electrical and thermal conductivity derivatives σ'/σ and κ'/κ (inset) creates a complicated dependence in the signs of the $\Gamma_{\pm}$ nonlinearity parameters, Equation (16), leading to alternating regions of LP (gray), EOC (blue), and LA\EOC (red). b) These regions, in turn, correspond to the PDR, NDR, and hysteresis regions in the steady-state curve. Examination of the voltage–current slope (inset) confirms the presence of EOC-NDR that enables self-oscillations. c) Steady-state voltage and current plotted as functions of channel temperature show that for the inaccessible LA\EOC PDR region within the electrical hysteresis, point A is at a lower temperature than point B.

also indirectly confirm LA-PDR within the electrical hysteresis. After the LA\EOC hysteresis region, the model predicts one more EOC/NDR region, followed by a final LP/PDR region, consistent with the data.

The differences between the modeled intra-channel, extra-channel, and net device I–V plots explain the dimension-dependent difference in ordering between the NDR onset and reverse hysteresis. Clearly, the effect of the extra-channel I–V contribution when added to the intra-channel contribution is to increase the net device current at fixed voltage, with the increase in current being greater at larger voltages, due to the self-heating of the extra-channel region. This causes the magnitude of the NDR slope for the net device I–V curve to increase substantially relative to the intra-channel I–V curve's NDR slope (Figure 3b). For the device (L = 10 µm, W = 10 µm) with mid-range dimensions, the increased net NDR slope is nearly vertical. However, for a device with a larger extra-channel I–V contribution, i.e., a wider device, the net NDR at high voltage was pushed to high enough current that the net I–V curve again was positively sloped, effectively increasing the current corresponding to the NDR. When this increase was large enough, the NDR onset was pushed above the reverse hysteresis threshold, as seen for the wider devices in Figure 3a. In contrast, varying the length did not have this effect—since the channel extends across the device length, a change in length scales the intra- and extra-channel I–V contributions identically. All the I–V curves in Figure 3b had the NDR onset below the reverse hysteresis threshold, despite having varying length. We also tested this hypothesized mechanism for independently shifting the NDR onset by scaling the extra-channel width in the model (with fixed intra-channel width) and found that we could recreate the shift, although the NDR onset was essentially equal to, instead of greater than, the reverse hysteresis threshold (Figure S8, Supporting Information).

4.4. Inferring Thermal and Electrical Capacitance from Oscillations

With respect to the device compact model Equations (2a) and (2b), the electrical and thermal conductances $G_{el}(T)$ and $G_{th}(T)$ have been satisfactorily measured and modeled, and only the determination of the thermal capacitance $C_{th}(T)$ and effective electrical capacitance C_{eff} remains. Equations (7a) and (7b) together with the computed nonlinearity parameters and the measured oscillation frequencies (Figure 4a,b) provide the final constraint. Fortunately, Equations (7a) and (7b) treat the two capacitance parameters independently: the shape (f/f_0) of the curve depends only on the electrical capacitance C_{eff} or c but is independent of thermal capacitance $C_{th}(T)$, and the scaling (f_0) of the curve depends only on $C_{th}(T)$. This helps greatly with the convergence and precision of the least-squares fitting procedure.

By fitting Equations (7a) and (7b) to the oscillation frequencies (**Figure 11**) measured on the device (L = 8 µm, W = 10 µm) in Figure 4, the best-fit capacitance values were obtained (**Table 4**), with a corresponding SER of 91.7 Hz, which is 0.6% of the full-scale range of 15 kHz. In this case, the number of data points (N = 22) was too small for the estimated Jacobian from the Matlab nlparci routine to provide accurate 95% confidence

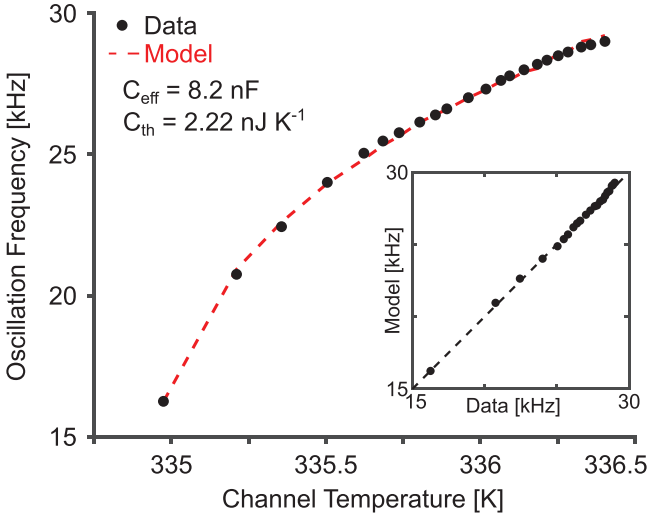

Figure 11. Determination of electrical and thermal capacitances using least-squares fitting to linearized frequency dependence Equations (7a) and (7b). For frequencies, uncertainties (standard deviation of 1M measured cycle periods) are less than 150 Hz.

intervals. Instead, the uncertainties were estimated by varying the parameters one at a time around their fitted values, and then determining what intervals lead to a 5% increase of the SER to ≈96 Hz.

Despite the thermal mapping, it is unclear what volume of the device contributes to the effective thermal capacitance above. Nonetheless, for consistency with the material-dependent electrical and thermal conductivity parameters, the thermal capacitance was normalized by the channel volume of $2.6 \times 0.1 \times 8$ (μm)^3 to yield a volumetric specific heat of

$$c_{th} \equiv C_{th}/\text{volume} = (1.07 \pm 0.4) \times 10^9 \text{ J m}^{-3} \text{ K}^{-1}.$$

This assumes that the actual volume contributing to the effective thermal capacitance is the intra-channel volume, based on the contribution of the martensitic FOPT latent heat; whereas the extra-channel region is much cooler than the transformation critical temperature. This volumetric heat capacity is nearly 140× larger than the baseline values for comparable VO_2 in the literature. However, it should be emphasized that the oscillation data used to fit C_{th} exist only in a narrow temperature regime near the FOPT, and substantial increases in heat capacity near FOPTs due to latent heat are expected.

Assuming the electrical capacitance C_{eff} is determined by the device structure and applying the parallel-plate capacitor equation,

$$C_{dev} = \varepsilon_r \varepsilon_0 \frac{WH}{L} \tag{18}$$

yields an unrealistic dielectric constant $\varepsilon_r \approx 10^{10}$. Therefore, Equation (18) suggests some substantial part of C_{eff} arises from the external source and line capacitance, and in fact, the value of 8.2 nF is roughly consistent with both line capacitance (≈ 6 m × 0.1 nF m^{-1}) and potential source unit capacitance (a 10 nF capacitor measuring a 100 μA current for 100 ms collection time outputs a useful voltage signal of 10 V). Thus C_{eff} is

Table 4. Compact model parameters for thermal capacitance (heat capacity) and effective electrical capacitance derived by fitting oscillation data in Figure 4 to Equations (7a) and (7b). Uncertainties are computed from estimated Jacobians using a 5% increase to the SER.

Electro-thermal Capacitance Parameters			
Parameter	Units	Fitted Value	Uncertainty
C_{eff}	[nF]	8.20	±0.03
C_{th}	[nJ K^{-1}]	2.22	±0.08

mainly due to the external circuit components, and since the current and voltage ranges were fixed for all measurements, we assumed that $C_{eff} = C_{ext} = 8.2$ nF is independent of device dimension.

Finally, the capacitance parameters have been fit using a rigorous but approximate linearization procedure. In order to demonstrate that the constructed model also accurately replicates the behavior of the nonlinear circuit, we simulated (**Figure 12**) the dynamical behavior of the model, again at the three bias points (i), (ii), (iii) for which the corresponding experimental data were presented in Figure 4b. Before simulating, the fitted thermal capacitance was given a small doubling correction to 4.4×10^{-9} JK^{-1} to provide better agreement with the oscillation frequency at (ii). The simulations have been performed over the interval $0 \le t \le 2$ ms and plotted for $1 \le t \le 2$ ms after all transients have disappeared.

The simulations show that the model oscillates at all three NDR biases, meaning that the fit electrical capacitance C_{eff} is larger than the critical capacitance, as it should be. There is quantitative agreement between the simulations in Figure 12a and the corresponding data in Figure 4b in terms of predicted oscillation frequencies (better than 10%) and oscillation shapes, particularly the spike followed by a sub-baseline voltage during the refraction period. However, the model predicts that the magnitude of the oscillations gradually decreases at higher bias; whereas experiment shows (Figure 4b) that the magnitude of the oscillations is mostly constant across the whole NDR region. The underlying thermal oscillations (Figure 12b) developed from the dynamical simulation suggest that the unobserved decrease in electrical oscillation magnitude is mostly driven by the thermal oscillation magnitude decreasing from 350 to 340 K, which corresponds to strong nonlinearities in $\sigma(T)$ and $\kappa(T)$. This, in turn, suggests that there is some feature in either the thermal capacitance or thermal conductivity functions that our model has not captured. For example, the thermal capacitance has here been assumed to be temperature-independent due to the relative sparsity of the dynamical data. However, $c_{th}(T)$ is likely strongly temperature-dependent around the FOPT.

5. Discussion: Materials Properties as Neuromorphic Design Constraints

The analysis of Section 4 revealed that both the electrical and thermal transport of VO_2 are highly nonlinear around the IMT, and it is this nonlinearity that provides it with the capability for NDR, instability, and oscillation. However, for materials selection and screening, it is necessary not only to

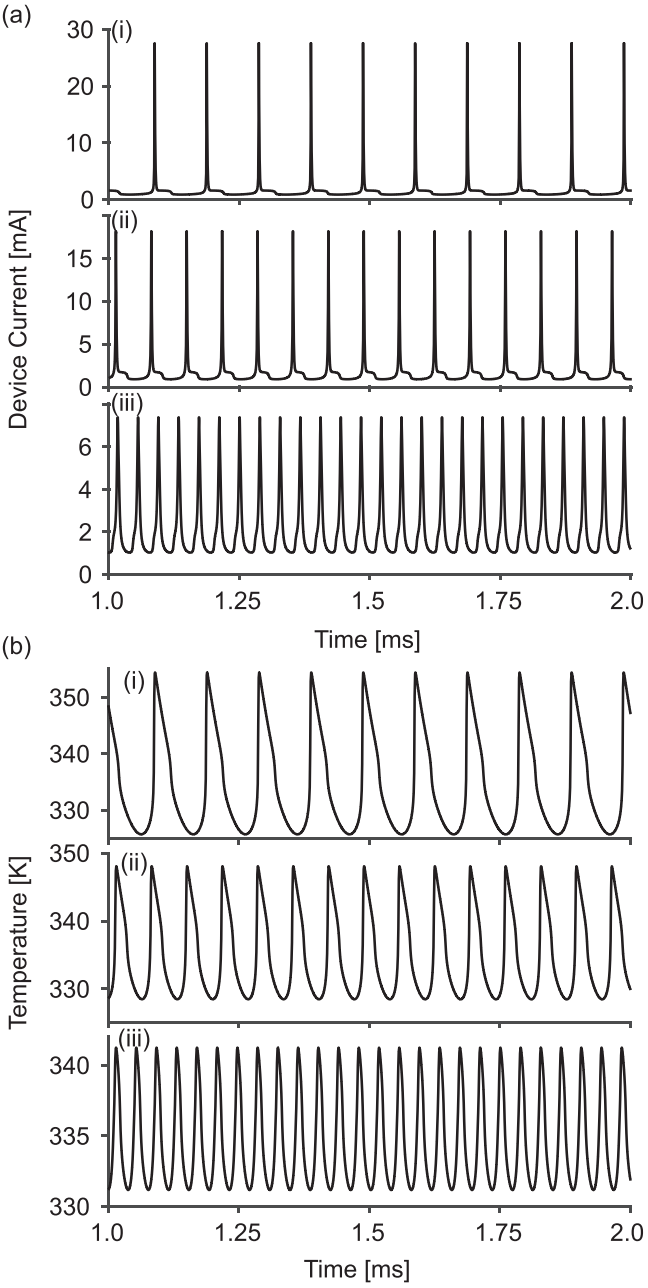

Figure 12. Numerically simulated electro-thermal oscillations evaluated at bias points (i), (ii), (iii) marked in Figure 4a. a) Simulated oscillations in electrical current, compare directly against oscillations in Figure 4b. b) Simulated oscillations in channel temperature.

accurately describe electro-thermal nonlinearity, but to quantify it and understand how it directly controls and constrains desired neuromorphic behavior. For example, NbO_2 is another memristor oxide with nonlinear electrical and thermal conductivities, but in contrast to VO_2, its IMT occurs far above room temperature, near 1080 K.[22] Near room temperature and far below 1080 K, the thermal conductivity of NbO_2 should be approximately constant, in direct contrast with VO_2, for which the thermal conductivity is a highly nonlinear, non-monotonic function. Well below its IMT, the electrical conductivity of NbO_2 is well-described by thermally activated transport,[23] of the form

$$\sigma(T) \propto \exp\left(-\frac{\varepsilon}{k_B}\left(\frac{1}{T}-\frac{1}{T_0}\right)\right) \tag{19}$$

with activation energy $\varepsilon \approx 0.3$–0.6 eV. The near room temperature electrical conductivity for NbO_2 Equation (19) is a weaker nonlinearity than for VO_2 (Equations (14a), (14b), and (14c)). As an illustration, for VO_2 studied here, $\sigma(T)$ increases by an order of magnitude between 331 and 338 K; whereas using Equation (19) with $\varepsilon = 0.45$ eV and $T_0 = 300$ K, the same order of magnitude increase in NbO_2 requires self-heating from 300 to 344 K, which is a temperature interval $6\times$ larger.

The larger electrical nonlinearity σ'/σ in VO_2 compared to NbO_2 leads directly to a larger nonlinearity parameter Γ_- (Equation (16)). Furthermore, in VO_2, the nonlinear interfacial thermal conductivity couples to the electrical nonlinearity, leading to a larger overall nonlinearity: Γ_- for VO_2 attains a maximum of 28 but would decrease to 13 K K^{-1} if the thermal nonlinearity was absent. Both of the electrical and thermal nonlinearities in NbO_2 near room temperature are substantially smaller. Applying the Γ_- definition (Equation (6)) to Equation (19) yields

$$\Gamma_-^{NbO_2}(T) = \frac{\varepsilon}{k_B T^2}(T-T_0)-1 \tag{20}$$

For $\varepsilon = 4.5$ eV and $T_0 = 300$ K, Equation (20) describing NbO_2 takes on a maximum of 2.43 within the near-room temperature interval 300 K $\le T \le$ 400 K, nearly an order of magnitude smaller than for VO_2.

The relationships between the nonlinearity parameter, minimal destabilizing capacitance (Equation (6)), and typical oscillation frequencies (Equation (7b)) then imply that, when biased within 100 K of room temperature and all else being equal, the VO_2 destabilizing capacitance is an order of magnitude smaller than NbO_2, and the resulting oscillations are an order of magnitude faster. This is an over-simplification: the destabilizing capacitance and oscillation frequencies depend on device dimension and baseline electrical and thermal conductivities in addition to the Γ_- nonlinearities. Furthermore, the analysis changes completely if NbO_2 is biased and operated near its IMT at 1080 K, although this is undesirable from the point of view of requiring active cooling to prevent overheating of neighboring components and passivation to prevent self-oxidation. However, this analysis begins to specify the tradeoffs between nonlinearity of electro-thermal transport versus other factors, and definitively links the high overall nonlinearity in VO_2 enabled by its coupled electrical and thermal nonlinearities to its potential for high-bandwidth neuromorphic behavior near room temperature. Together with device dimension, baseline absolute conductivity, and external circuit constraints, the nonlinearity parameters constitute a major design consideration when selecting a material for a particular neuromorphic application.

The presence of large coupled electrical and thermal nonlinearities in VO_2 is also a double-edged sword. The large thermal nonlinearity increases the overall nonlinearity, but

this eventually creates such a large instability that local oscillations are no longer possible; the locally unstable NDR collapses and becomes globally unstable PDR within the hysteresis feature (Figure 10a,b). Although the large negative thermal nonlinearity increases the slope of the NDR region, it simultaneously creates a relatively low upper bound for NDR in terms of electrical bias, at which point the system changes from useful EOC-NDR to LA/EOC-PDR. This means that oscillations in the present VO_2 devices are only possible in the small temperature interval between 334 and 336.5 K; whereas Equation (20) (T: $\Gamma_{\pm}(T) \geq 0$) implies NbO_2 can oscillate everywhere between 318.8 and 1080 K, at which point its large thermal nonlinearities at high temperature also induce unstable PDR. All else being equal, especially device dimensions, this translates directly into a larger NDR region on the I–V curve for NbO_2. In this sense, VO_2 memristors, or at least the undoped VO_2/SiN devices studied here, have a more limited range of parameter space within which they can be biased to make them capable for neuromorphic applications, as a direct result of their large thermal nonlinearities near room temperature.

6. Conclusion

Using concepts and equations derived from the theory of local activity, we have developed a systematic procedure for fitting a robust model to quasistatic and dynamic electrical and in situ thermal data. The procedure yields a compact model expressed entirely in terms of material properties, natural device scaling laws, and a single inferred external electrical capacitor, which is systematically fit step by step to a minimal data set. Furthermore, the model is informed by data from multiple independent devices, and satisfactorily reproduces quasistatic and dynamical data on an individual device. The electro-thermal characterization developed during this process agrees well with previous estimates of electrical and thermal conductivity and capacitance, and also points toward as-yet unexplored thermal physics. In this way, the compact model is predictive and falsifiable.

The systematic local-activity-based modeling procedure has led to several important lessons. First, the model's general success for a variety of data validates the initial hypothesis that the wide range of static and dynamic data produced by nonlinear Mott switches is ultimately due to the interaction between fixed material properties, scaling laws, and dynamical equations. It is the interaction among these that we vary when performing experiments (e.g., changing DC bias), but the properties and equations themselves do not change. Essentially the same temperature-dependent electrical conductivity is measured regardless of whether it is characterized with low-power, isothermal uniform conduction or with high-power localized conduction, and we expect the same to be true of the interfacial thermal conductivity, paving the way for future work with independent thermal characterization of the electro-thermal properties.

Second, the model depends crucially on the Ridley bifurcation phenomenon, which partitions the device volume into a hot channel and cool exterior volume. In this work, a specialized thermoreflectance technique was used to directly measure the temperature and image the morphology of the hot channel; however, it is unlikely such techniques would be available on an industrial scale. This alone provides an impetus to further develop non-equilibrium steady-state thermodynamics to be able to predict the channel properties from first principles alone. The difference in channel morphology between devices with different dimensions may be the origin of the material-dependent compact model is not quite portable in describing other on-chip devices (Figures S8 and S9, Supporting Information).

Finally, we have made several initial steps toward understanding how electro-thermal properties of VO_2/SiN devices contribute to their potential for desired dynamical behavior, and especially how they might compare to other thermal memristors. The peculiar features of these VO_2 devices are extremely large electrical and thermal nonlinearities accompanying the FOPT, which are highly coupled. This in turn leads to a steep NDR with a small critical capacitance that exists only over a narrow temperature interval. In contrast, for NbO_2 devices the electrical and thermal nonlinearities are decoupled, and the electrical nonlinearity is substantially weaker. This leads to a shallow NDR, but a much larger NDR temperature interval. In both cases, a rapidly decreasing thermal conductivity plays a central role in creating undesired global instability and limiting the accessible NDR region, and so understanding the physics underlying this thermal nonlinearity is crucial to future development. As noted in Section 3, the dynamical criteria determined by application of local activity theory depend only indirectly on transport physics, intrinsic material properties, and device configuration. Hence, the entire body of literature on engineering electro-thermal transport in VO_2—doping, defects, vacancies, strain, crystallinity, etc.—are all immediately relevant tuning knobs for the targeted design of VO_2 memristors for neuromorphic applications.[24] Furthermore, vertically stacked structures with higher device densities may be used equally well as the present lateral devices; the lateral architecture is required here for thermoreflectance mapping. The only criterion is that the resultant electro-thermal conductivity functions are sufficiently nonlinear in the sense outlined in Section 3.

In summary, we have used the principles of local activity to develop systematic procedures and principles for both extracting electro-thermal transport properties from a synthesis of steady-state and dynamic data, and subsequently analyzing the electro-thermal properties to understand their direct relation to desired neuromorphic applications. With these advances in modeling and relating material to neuromorphic properties, we have provided a major step toward systematic, fast, portable device modeling that contributes to the foundation for industrial-scale design and synthesis of neuromorphic networks.

7. Experimental Section

Lateral vanadium dioxide devices were patterned from a 100 nm blanket film grown on silicon nitride substrate by pulsed laser deposition (PLD). See refs. [25] for additional details. Devices were patterned into horizontal bars using a dry CF_4/Ar etching process, then e-beam evaporating 100 nm of Al followed by 400 nm of Pd top contacts for top contacts to define device dimensions. Raman shift spectra were taken using a commercial Horiba LabRam HR bench top confocal microscope system, counting for 300 s at 0.5% intensity.

Raman spectroscopy data from different temperatures were aligned by subtracting the mean intensity between 540–560 cm^{-1} (far from both the SiN substrate and VO_2 M1 peaks), then a small linear baseline that was fit to the highest temperature (343 K) data was identically subtracted from the others. Slight shifts along the abscissa due to grating zero position were compensated by setting the Si substrate at 520 cm^{-1}.

Conductivity–temperature (σ–T) and continuous quasistatic DC current–voltage curves were measured using a Keysight B1500A Semiconductor Device Analyzer equipped with Medium-Current Source Measure Unit (MCSMU) cards. σ–T curves were generated by fixing the external temperature with a temperature stage and pointwise averaging five linear I–V curves before obtaining an average slope. In situ Joule self-heating was mitigated by using low-power (V_{max} < 150 mV), low-resolution (30–40 points) measurements with the SMU cards operated in high speed (HS) mode for fast acquisition (0.5 s per curve). This procedure was intentionally used in place of the more typical method of applying a constant DC current, reading the voltage and computing the ratio, since with that method, it is not possible to verify the measurement is taken under linear, low-power conditions such that self-heating is negligible.

Continuous quasi-DC curves were obtained with the B1500A in high resolution (HR) mode using long wait times (>300 ms per point) between setpoint change and acquisition, in combination with long averaging times (>20 PLC = 340 ms), in order to mitigate the effect of transient and persistent oscillations around the desired true I–V steady states. Pointwise quasi-DC curves were measured using a Keysight B2901A benchtop Source Measure Unit with >500 ms wait time and >500 ms averaging. Each pointwise I–V point was obtained by averaging >4 triggered measurements over one minute at each fixed current setpoint. Persistent self-oscillations in the negative differential resistance region were recorded using a Keysight DSOS104A oscilloscope with a calibrated active N2818A differential probe.

Quasistatic device channel temperatures were derived from a Microsanj differential Thermal Image Analyzer (TIA), with 10 s averaging time and 20 s cool-down time, after calibrating the reflectivity–temperature curve as described in the Supporting Information. In every case, an appropriately sized resistor was placed in series with the VO_2 lateral device before characterization, providing: 1) a convenient constant impedance probing point to avoid loading the oscilloscope and 2) damping of large electro-thermal oscillations in the NDR region for which the thermal component otherwise fatigues or destroys the devices during attempted characterization. The Microsanj necessitated measurement of thermoreflectance maps in differential mode, i.e., synchronized between power-off and power-on states. This was accomplished by using the Microsanj trigger out signal to control an electromagnetic relay, thereby periodically load switching the SMU power output between the VO_2 DUT during ON collection and a peripheral 1kΩ resistor during OFF collection. Hence, the benchtop B2901A SMU that could tolerate repeated load switching over long times at fixed bias was required.

Statistical Analysis: A variety of data collection and computations were performed throughout this work, leading to a variety of methods for determining data uncertainties. For single measurements (e.g., continuous I–V sweeps and oscilloscope traces), manufacturer specifications or instrument noise floor were used as the uncertainty. For multiple consecutive measurements (e.g., spot I–V and spot thermoreflectance measurements), the measurement was determined as (mean ± standard deviation). In nearly every case, averaging multiple measurements yields uncertainties that are so small relative to the full scale of the plots displayed as to not be meaningfully visible. For this reason, the uncertainties are stated in the figure captions. For linear and nonlinear parametric fits to data (e.g., the tables of parameters for electrical and thermal conductance), the uncertainty is computed using the Jacobian of the error with respect to the fitting parameters, computed with the nlparci() function in MATLAB. No other statistical tests (e.g., t-test, hypothesis testing) beyond linear and nonlinear parametric fitting were performed.

Supporting Information

Supporting Information is available from the Wiley Online Library or from the author.

Acknowledgements

Blanket films of VO_2 were grown by Kechao Tang then of U.C. Berkeley, now of Peking University. Device fabrication was performed at the Stanford Nanofabrication Facility and the Stanford Nano Shared Facilities, supported by the National Science Foundation (NSF) under award ECCS-1542152. T.D.B and R.S.W were supported by the X-Grants Program of the President's Excellence Fund at Texas A&M University. T.D.B. and S.K. were supported by the Laboratory Directed Research and Development programme at Sandia National Laboratories, a multi-mission laboratory managed and operated by National Technology and Engineering Solutions of Sandia, LLC, a wholly-owned subsidiary of Honeywell International Inc., for the U.S. Department of Energy's National Nuclear Security Administration under contract DE-NA0003525. S.B, M.I., and E.P. were supported in part by ON Semiconductor and the Stanford SystemX Alliance. S.B. and M.I. acknowledge support from the Stanford Graduate Fellowship (SGF) program and the NSERC Postgraduate Scholarship program. This paper describes objective technical results and analysis. Any subjective views or opinions that might be expressed in the paper do not necessarily represent the views of the U.S. Department of Energy or the United States Government. This article has been authored by an employee of National Technology & Engineering Solutions of Sandia, LLC under Contract No. DE-NA0003525 with the U.S. Department of Energy (DOE). The employee owns all right, title and interest in and to the article and is solely responsible for its contents. The United States Government retains and the publisher, by accepting the article for publication, acknowledges that the United States Government retains a non-exclusive, paid-up, irrevocable, world-wide license to publish or reproduce the published form of this article or allow others to do so, for United States Government purposes. The DOE will provide public access to these results of federally sponsored research in accordance with the DOE Public Access Plan https://www.energy.gov/downloads/doe-public-access-plan.

Conflict of Interest

The authors declare no conflict of interest.

Data Availability Statement

The data that supports the findings of this study are available in the supplementary material of this article.

Keywords

local activity, memristors, neuromorphic devices, nonlinear dynamics, vanadium dioxide

Received: June 15, 2022
Revised: August 23, 2022
Published online: November 3, 2022

[1] a) S. Kumar, X. Wang, J. P. Strachan, Y. Yang, W. D. Lu, *Nat. Rev. Mater.* **2022**, *7*, 575; b) S. Bohaichuk, S. Kumar, in *Memristive Devices for Brain-Inspired Computing* (Eds: S. Spiga, A. Sebastian,

D. Querlioz, B. Rajendran), Woodhead Publishing, Sawston, UK **2020**; c) J. D. Kendall, S. Kumar, *Appl. Phys. Rev.* **2020**, *7*, 011305; d) X. Zhang, A. Huang, Q. Hu, Z. Xiao, P. K. Chu, *Phys. Status Solidi A* **2018**, *215*, 1700875; e) F.-X. Liang, I. T. Wang, T.-H. Hou, *Adv. Intell. Syst.* **2021**, *3*, 2100007; f) D. S. Jeong, K. M. Kim, S. Kim, B. J. Choi, C. S. Hwang, *Adv. Electron. Mater.* **2016**, *2*, 1600090; g) D. Liu, H. Yu, Y. Chai, *Adv. Intell. Syst.* **2021**, *3*, 2000150; h) G. Zhou, Z. Wang, B. Sun, F. Zhou, L. Sun, H. Zhao, X. Hu, X. Peng, J. Yan, H. Wang, W. Wang, J. Li, B. Yan, D. Kuang, Y. Wang, L. Wang, S. Duan, *Adv. Electron. Mater.* **2022**, *8*, 2101127; i) R. Yang, H.-M. Huang, X. Guo, *Adv. Electron. Mater.* **2019**, *5*, 1900287.

[2] a) Y. Ke, S. Wang, G. Liu, M. Li, T. J. White, Y. Long, *Small* **2018**, *14*, 1802025; b) A. Bradicich, H. Clarke, E. J. Braham, A. Yano, D. Sellers, S. Banerjee, P. J. Shamberger, *Adv. Electron. Mater.* **2022**, *8*, 2100932; c) J. L. Andrews, D. A. Santos, M. Meyyappan, R. S. Williams, S. Banerjee, *Trends Chem.* **2019**, *1*, 711; d) L. Gao, P.-Y. Chen, S. Yu, *Appl. Phys. Lett.* **2017**, *111*, 103503.

[3] W. Yi, K. K. Tsang, S. K. Lam, X. Bai, J. A. Crowell, E. A. Flores, *Nat. Commun.* **2018**, *9*, 4661.

[4] M. Hu, C. E. Graves, C. Li, Y. Li, N. Ge, E. Montgomery, N. Davila, H. Jiang, R. S. Williams, J. J. Yang, Q. Xia, J. P. Strachan, *Adv. Mater.* **2018**, *30*, 1705914.

[5] a) T. D. Brown, S. Kumar, R. S. Williams, *Appl. Phys. Rev.* **2022**, *9*, 011308; b) A. Ascoli, A. S. Demirkol, R. Tetzlaff, S. Slesazeck, T. Mikolajick, L. O. Chua, *Front. Neurosci.* **2021**, *15*, 651452.

[6] S. Kumar, G. Gibson, C. E. Graves, M. D. Pickett, J. P. Strachan, R. S. Williams, in *Handbook of Memristor Networks* (Eds: L. Chua, G. C. Sirakoulis, A. Adamatzky), Springer International Publishing, Cham, Switzerland **2019**.

[7] a) L. O. Chua, *Introduction to Nonlinear Network Theory*, McGraw-Hill, New York **1969**; b) L. O. Chua, *IEEE Trans. Circuits Syst.* **1980**, *27*, 1014; c) S.-i. Yi, A. A. Talin, M. J. Marinella, R. S. Williams, *Adv. Intell. Syst.* **2022**, *4*, 2200070.

[8] a) L. O. Chua, *Int. J. Bifurcation Chaos Appl. Sci. Eng.* **2005**, *15*, 3435; b) L. O. Chua, *IEEE Trans. Circuits Syst.* **1999**, *46*, 71; c) K. Mainzer, in *Chaos, CNN, Memristors and Beyond*, World Scientific, Singapore **2012**.

[9] I. Messaris, T. D. Brown, A. S. Demirkol, A. Ascoli, M. M. A. Chawa, R. S. Williams, R. Tetzlaff, L. O. Chua, *IEEE Trans. Circuits Syst.* **2021**, *68*, 4979.

[10] a) S. M. Bohaichuk, S. Kumar, G. Pitner, C. J. McClellan, J. Jeong, M. G. Samant, H. S. P. Wong, S. S. P. Parkin, R. S. Williams, E. Pop, *Nano Lett.* **2019**, *19*, 6751; b) S. M. Bohaichuk, S. Kumar, M. M. Rojo, R. S. Williams, M. Islam, G. Pitner, J. Jeong, M. G. Samant, S. S. P. Parkin, E. Pop, ArXiv: 2012.07943, **2020**.

[11] a) M. D. Pickett, D. B. Strukov, J. L. Borghetti, J. J. Yang, G. S. Snider, D. R. Stewart, R. S. Williams, *J. Appl. Phys.* **2009**, *106*, 074508; b) S. Kumar, R. S. Williams, Z. Wang, *Nature* **2020**, *585*, 518; c) J. P. Strachan, A. C. Torrezan, F. Miao, M. D. Pickett, J. J. Yang, W. Yi, G. Medeiros-Ribeiro, R. S. Williams, *IEEE Trans. Electron Devices* **2013**, *60*, 2194; d) D. B. Strukov, G. S. Snider, D. R. Stewart, R. S. Williams, *Nature* **2008**, *453*, 80; e) Y. Zhuo, R. Midya, W. Song, Z. Wang, S. Asapu, M. Rao, P. Lin, H. Jiang, Q. Xia, R. S. Williams, J. J. Yang, *Adv. Electron. Mater.* **2021**, *8*, 2100696.

[12] S. Kumar, R. S. Williams, *Nat. Commun.* **2018**, *9*, 2030.

[13] a) M. Taha, S. Walia, T. Ahmed, D. Headland, W. Withayachumnankul, S. Sriram, M. Bhaskaran, *Sci. Rep.* **2017**, *7*, 17899; b) J. Zhang, Z. Zhao, J. Li, H. Jin, F. Rehman, P. Chen, Y. Jiang, C. Chen, M. Cao, Y. Zhao, *ACS Appl. Mater. Interfaces* **2017**, *9*, 27135; c) C. Chen, Y. Zhao, X. Pan, V. Kuryatkov, A. Bernussi, M. Holtz, Z. Fan, *J. Appl. Phys.* **2011**, *110*, 023707; d) V. Théry, A. Boulle, A. Crunteanu, J. C. Orlianges, A. Beaumont, R. Mayet, A. Mennai, F. Cosset, A. Bessaudou, M. Fabert, *J. Appl. Phys.* **2017**, *121*, 055303.

[14] a) Z. I. Mannan, H. Choi, H. Kim, *Int. J. Bifurcat. Chaos* **2016**, 26; b) A. Ascoli, S. Slesazeck, H. Mähne, R. Tetzlaff, T. Mikolajick, *IEEE Trans. Circuits Syst.* **2015**, *62*, 1165.

[15] B. K. Ridley, *Proc. Phys. Soc.* **1963**, *82*, 954.

[16] S. Kumar, M. D. Pickett, J. P. Strachan, G. Gibson, Y. Nishi, R. S. Williams, *Adv. Mater.* **2013**, *25*, 6128.

[17] L. O. Chua, *Proc. IEEE* **2003**, *9*, 1830.

[18] a) L. Chua, *IEEE Trans. Circuit Theory* **1971**, *18*, 507; b) L. Chua, presented at *Int. Photonics Optoelectron. Meet.*, Wuhan, China, November **2017**; c) L. Chua, V. Sbitnev, H. Kim, *Int. J. Bifurcat. Chaos* **2012**, *22*, 1230011; d) L. O. Chua, K. S. Mo, *Proc. IEEE* **1976**, *64*, 209.

[19] G. A. Gibson, *Adv. Funct. Mater.* **2018**, 28.

[20] S. H. Strogatz, *Nonlinear Dynamics and Chaos : With Applications to Physics, Biology, Chemistry, and Engineering*, 2nd ed., Westview Press, Boulder, CO, USA **2015**.

[21] a) J. Hu, Y. P. Chen, *Phys. Rev. E* **2013**, *87*, 062104; b) F. Li, J. Wang, G. Xia, *J. Phys. Chem. C* **2020**, *124*, 92; c) J. Ren, J.-X. Zhu, *Phys. Rev. B* **2013**, *87*, 241412; d) Y. Yang, D. Ma, Y. Zhao, L. Zhang, *J. Appl. Phys.* **2020**, *127*, 195301.

[22] a) Y. Sakai, N. Tsuda, T. Sakata, *J. Phys. Soc. Jpn.* **1985**, *54*, 1514; b) J. A. Roberson, R. A. Rapp, *J. Phys. Chem. Solids* **1969**, *30*, 1119.

[23] I. Messaris, R. Tetzlaff, A. Ascoli, R. S. Williams, S. Kumar, L. Chua, in *2020 IEEE Int. Symp. on Circuits and Systems (ISCAS)*, IEEE, Piscataway, NJ, USA **2020**, https://doi.org/10.1109/ISCAS45731.2020.9181036.

[24] a) Y. Cui, Y. Ke, C. Liu, Z. Chen, N. Wang, L. Zhang, Y. Zhou, S. Wang, Y. Gao, Y. Long, *Joule* **2018**, *2*, 1707; b) M. Kamalisarvestani, R. Saidur, S. Mekhilef, F. S. Javadi, *Renewable Sustainable Energy Rev.* **2013**, *26*, 353; c) M. Li, S. Magdassi, Y. Gao, Y. Long, *Small* **2017**, *13*, 1701147; d) D. Nunes, A. Pimentel, A. Gonçalves, S. Pereira, R. Branquinho, P. Barquinha, E. Fortunato, R. Martins, *Semicond. Sci. Technol.* **2019**, *34*, 043001; e) S. Wang, M. Liu, L. Kong, Y. Long, X. Jiang, A. Yu, *Prog. Mater. Sci.* **2016**, *81*, 1.

[25] a) S. Abedini Dereshgi, M. C. Larciprete, M. Centini, A. A. Murthy, K. Tang, J. Wu, V. P. Dravid, K. Aydin, *ACS Appl. Mater. Interfaces* **2021**, *13*, 48981; b) M. C. Larciprete, M. Centini, S. Paoloni, S. A. Dereshgi, K. Tang, J. Wu, K. Aydin, *Opt. Express* **2020**, *28*, 39203; c) M. C. Larciprete, M. Centini, S. Paoloni, I. Fratoddi, S. A. Dereshgi, K. Tang, J. Wu, K. Aydin, *Sci. Rep.* **2020**, *10*, 11544.